

1

[ATLAS Semivisible Jets]

2

[Elena Laura Busch]

3

Submitted in partial fulfillment of the
requirements for the degree of
Doctor of Philosophy
under the Executive Committee
of the Graduate School of Arts and Sciences

4

5

6

7

8

COLUMBIA UNIVERSITY

9

2024

10

© 2024

11

[Elena Laura Busch]

12

All Rights Reserved

13

Abstract

14

[ATLAS Semivisible Jets]

15

[Elena Laura Busch]

16

Abstract of dissertation (place-holder).

Table of Contents

18	Acknowledgments	ix
19	Dedication	x
20	Introduction or Preface	1
21	I Theory	2
22	Chapter 1: The Standard Model	3
23	1.1 Phenomenology: Particles and Forces	3
24	1.1.1 Particles	3
25	1.1.2 Forces	4
26	1.2 QCD and Jets	7
27	1.3 Symmetries	8
28	1.3.1 Spontaneous Symmetry Breaking and The Higgs Mechanism	9
29	1.4 Experimental Validation of the Standard Model	10
30	1.5 Limitations of the Standard Model	11
31	Chapter 2: Physics Beyond the Standard Model	13
32	2.1 Hidden Valley Models	13
33	2.2 Dark QCD	14

34	2.3 Semi-visible Jets	15
35	II Experiment	17
36	Chapter 3: The Large Hadron Collider	18
37	3.1 Accelerator Physics	19
38	3.1.1 The Journey of a Proton	19
39	3.1.2 Magnets	20
40	3.2 Luminosity	21
41	3.3 LHC Timeline	24
42	Chapter 4: The ATLAS Detector	26
43	4.1 Coordinate System and Geometry	26
44	4.2 Inner Detector	28
45	4.2.1 Pixel Detector	28
46	4.2.2 Semiconductor Tracker	29
47	4.2.3 Transition Radiation Tracker	29
48	4.3 Calorimeters	30
49	4.3.1 Liquid Argon Calorimeter	31
50	4.3.2 Tile Calorimeter	34
51	4.4 Muon Spectrometer	35
52	4.5 Magnet System	37
53	4.6 Forward Detectors	38
54	4.7 Trigger and Data Acquisition	39

55	Chapter 5: Particle Reconstruction and Identification	41
56	5.1 Inner Detector Tracks	41
57	5.2 Photons and Electrons	42
58	5.3 Muons	44
59	5.4 Jets	46
60	5.4.1 Calorimeter Clusters	47
61	5.4.2 Particle Flow Algorithm	48
62	5.4.3 Jet Clustering	49
63	5.4.4 Ghost Track Association	52
64	5.5 Missing Transverse Energy	53
65	III Search	55
66	Chapter 6: Machine Learning Tools	56
67	6.0.1 Particle Flow Network (Supervised)	56
68	6.0.2 ANTELOPE (Semi-supervised)	67
69	Chapter 7: Monte Carlo and Data	74
70	Conclusion or Epilogue	75
71	References	79
72	Appendix A: Experimental Equipment	84
73	Appendix B: Data Processing	85

List of Figures

75	1.1	Diagram of the 17 particles comprising the Standard Model	4
76	1.2	Fundamental particle interactions of the three fundamental forces described by the Standard Model [2].	6
77			
78	1.3	An example Feynmann diagram of jet production	7
79	1.4	An illustration of the “hat shaped” potential of the Higgs field, resulting in a non-zero vacuum expectation value.	9
80			
81	2.1	Illustration of the hidden valley potential	14
82	2.2	The massive mediator particle Z' of the s-channel realization of a HV model	14
83	3.1	The LHC accelerator complex at CERN [27]	20
84	3.2	The octants of the LHC and location of various beam activities [26]. Stars indicate the locations of beam collisions, and the associated detectors recording the outcome of those collisions.	21
85			
86			
87	3.3	(Left) Total integrated luminosity over the course of Run 2. (Right) Average number of $p p$ interactions per bunch crossing in Run 2. Each curve is weighted by the integrated luminosity for the year.	23
88			
89			
90	3.4	Timeline of LHC and HL-LHC activities [29]. Integrated luminosity estimates are approximate, and not reflective of the exact amount delivered to each experiment. .	25
91			
92	4.1	ATLAS coordinate system and geometry	28
93	4.2	A 3D visualization of the structure of the ID in the barrel region [33]	29
94	4.3	ATLAS calorimetery system [34]	30

95	4.4	Diagram of a segment of the EMB, demonstrating the accordion plate arrangement [35]	32
97	4.5	A LAr pulse as produced in the detector (triangle) and after shaping (curve) [35]	33
98	4.6	Readout gap structure in HEC [35]	33
99	4.7	TileCal wedge module [38]	35
100	4.8	Cross section view of the muon spectrometer system [39]	36
101	4.9	Layout of the barrel and endcap toroid magnets [32]	38
102	5.1	Graphic illustrating the various objects and high level features identified by ATLAS object reconstruction, and their interaction with different systems of the ATLAS detector [42]	42
105	5.2	Track reconstruction seeding, finding and fitting illustration [43]	43
106	5.3	Three types of EM object candidates [45].	44
107	5.4	Four types of muon track candidates [47].	46
108	5.5	The fragmentation and hadronization processes undergone by a quark produced in a proton-proton collision [49].	47
110	5.6	A flow chart illustrating the particle flow algorithm progression [54].	50
111	5.7	A comparison of jet clustering with four different jet algorithms. The anti- k_t algorithm is observed to create the most conical jets, where the shape of the jet is immune to the presence of soft radiation [50].	51
114	5.8	A comparison of MC simulation and data for $Z \rightarrow \mu\mu$ events where real $E_T^{\text{miss}} = 0$ [61]. The resolution of the missing energy in the transverse ($x - y$) plane is observed to increase with increasing total $\sum E_T$	54
117	6.1	The Energy/Particle Flow Network concept, from Ref. [pfn].	57
118	6.2	An annotated diagram of the PFN architecture.	58
119	6.3	Distributions of the track multiplicity in the leading and subleading jets, comparing signal and background PFN training samples.	58

121	6.4 A diagram demonstrating how the two jet system is rotated in (ϕ, η)	59
122	6.5 The 7 PFN track variables in data and background MC, after the scaling and rota-	
123	tion procedure is applied. We see excellent modeling of the data by the MC within	
124	the track variables.	60
125	6.6 The 7 PFN track variables in background MC and signal MC. We see some differ-	
126	ences between signal and background, but the track kinematics are largely similar.	
127	61
128	6.7 PFN score for background MC, data, and signal, comparing a PFN training on	
129	QCD-only vs all-background MC samples. The average AUC for the QCD-only	
130	training (left) is 0.93, while the average AUC for the mixed background training	
131	(right) is 0.84. The sensitivity estimate across the grid is better for the QCD-only	
132	training - from the distribution we can conclude that this is because the sensitivity	
133	to MET enhanced signals is greatly reduced.	62
134	6.8 PFN architecture loss during training as a function of epoch (left) and the evaluated	
135	loss over the signal and background (right).	63
136	6.9 ROC the PFN score for combined signal (true positive) and QCD background (false	
137	positive).	64
138	6.10 AUC from the PFN score for each signal in the SVJ grid, shown versus the QCD-	
139	only training sample.	65
140	6.11 PFN score for two signals and the total background MC (top), and between data	
141	and MC (bottom). The difference between data and MC efficiency is minimal (<	
142	5%).	66
143	6.12 A visual representation of the 64 PFN latent space variables which create the input	
144	of the VAE component of ANTELOPE. The left shows a 2D histogram of the PFN	
145	latent space index (0-63) versus the value assumed by that index. The right shows	
146	1D histograms of two particular PFN latent space variables.	68
147	6.13 An annotated diagram of the ANTELOPE architecture.	69
148	6.14 ANTELOPE architecture loss during training as a function of epoch.	69
149	6.15 ANTELOPE score distribution comparing data and the total background MC (left),	
150	with good agreement observed between data and simulated background, and com-	
151	paring all background MC to signals (right), revealing good discrimination power.	
152	70
153	6.16 AUC from the ANTELOPE score for each signal in the SVJ grid.	71

154	6.17 Comparing data and the alternate signal models for the PFN score (top left), AN-	
155	TELOPE score (top right), E_T^{miss} (bottom left), and m_T (bottom right). The emerg-	
156	ing jet signal is an example of the gain of the model-independent ANTELOPE ap-	
157	proach, where it has a bimodal shape in PFN score but is clearly tagged as anom-	
158	alous by ANTELOPE.	72
159	6.18 Comparing data and the alternate signal models in terms of sensitivity (S/\sqrt{B}) for	
160	the PFN and ANTELOPE tools, applying the selection that is used in the analysis.	
161	The ANTELOPE network is found to provide significant added sensitivity to alter-	
162	nate signals such as the gluino \rightarrow R-hadron and emerging jets, which have higher	
163	E_T^{miss} than the SVJs.	73

List of Tables

165

Acknowledgements

166 Insert your acknowledgements text here. This page is optional, you may delete it if not

167 needed.

168

Dedication

169

Dedicated to my friends and family

170

Introduction or Preface

171 Insert your preface text here if applicable. This page is optional, you may delete it if not
172 needed. If you delete this page make sure to move page counter comment in thesis.tex to correct
173 location.

174

Part I

175

Theory

Chapter 1: The Standard Model

178 The Standard Model of particle physics is a universally accepted framework which explains
 179 the interactions of fundamental particles. All known fundamental particles, outlined in Figure
 180 1.1, are represented in the Standard Model. The model describes three of the four known forces:
 181 the electromagnetic force, the weak force, and the strong force. Gravity, the fourth fundamental
 182 force, is not addressed by the Standard Model. The Standard Model was primarily developed over
 183 the course of the 1960s and 1970s, by combining the work of many physicists into one coherent
 184 model. The Standard Model has been established as a well-tested theory by decades of experimen-
 185 tal physics research.

186 This chapter will seek to introduce the phenomenology and mathematical foundations of the
 187 Standard Model, and present the supporting experimental evidence. Phenomenon which are unex-
 188 plained by the Standard Model such as gravity will be considered at the end of the chapter, leading
 189 to an exploration of theories beyond the Standard Model in the subsequent chapter.

190 **1.1 Phenomenology: Particles and Forces**

191 1.1.1 Particles

192 A classic representation of the particles comprising the Standard Model is shown in Figure
 193 1.1. The two primary particles classes are bosons (gauge bosons and the scalar Higgs boson) and
 194 fermions (leptons and quarks). The bosons are carriers of fundamental forces, while the fermions
 195 are the building blocks of matter. Fermions are sorted into three *generations*, and each fermion is
 196 identified by a unique *flavor*.

197 Each entry in the table in Figure 1.1 is accompanied by 3 characteristic numbers: mass, charge,
 198 and spin. The mass of each particle is determined to limited precision by experimental observa-

Standard Model of Elementary Particles

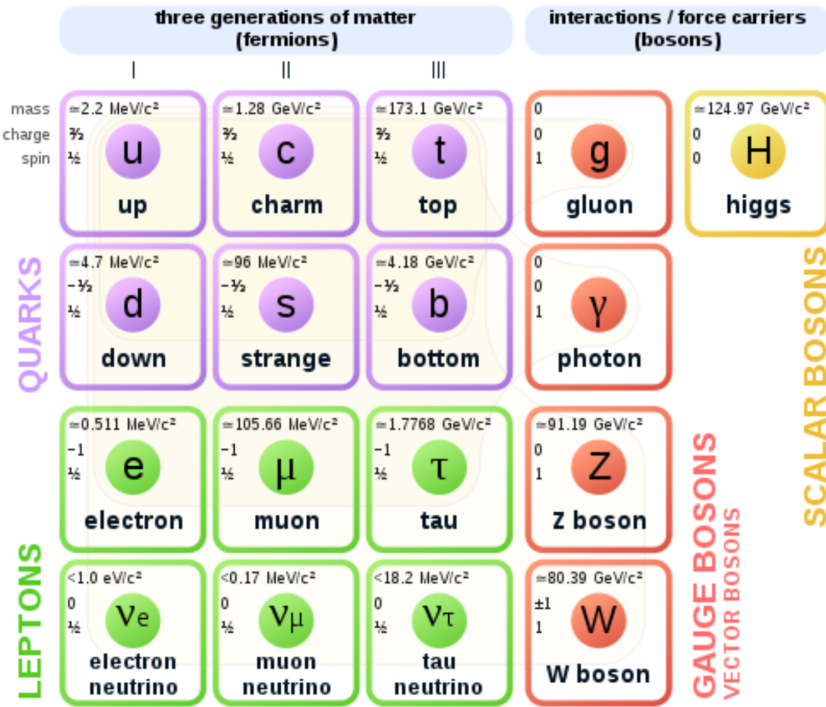


Figure 1.1: Diagram of the 17 particles comprising the Standard Model

199 tion, with the exception of photons and gluons which are known to be massless. Charge refers to
 200 the electromagnetic charge in the case of leptons and W bosons, and to color charge in the case
 201 of quarks and gluons. Spin is an intrinsic form of angular momentum carried by fundamental
 202 particles; all fermions have half integer spin, while bosons have integer spin.

203 Each particle is also known to have an *antiparticle*. Each antiparticle has the same mass but the
 204 opposite charge of their Standard Model counter part; for example, the antiparticle of the electron
 205 is the positron, which has all the same properties but a positive charge. The photon, Z boson,
 206 and Higgs are each their own antiparticle. The nature of antineutrinos is an open question driving
 207 neutrino physics research, as it is not currently known whether neutrinos are their own antiparticle.

208 1.1.2 Forces

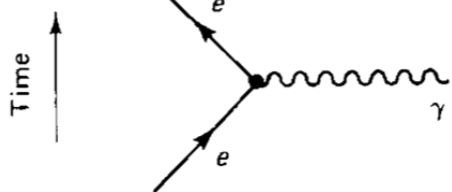
209 The three fundamental forces explained by the Standard Model are the electromagnetic force,
 210 the strong force, and the weak force. The photon is the carrier of the electromagnetic force, which

211 dictates the nature of interactions between electrically charged particles, and is widely covered by
212 introductory physics courses. The electromagnetic force has an infinite interaction range, a result
213 of the massless and non-self interaction nature of the photon. The electromagnetic interaction is
214 described by the theory of quantum electrodynamics (QED).

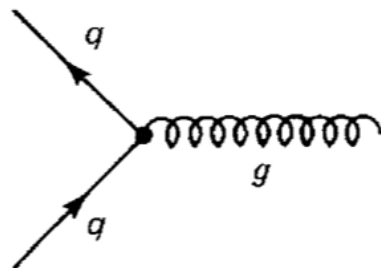
215 The weak force gives rise to atomic radiation and decay. It allows for the processes of beta
216 decay, which enables conversion between neutrons and protons within the nucleus of an atom. In
217 the process of beta decay, a proton decays into a neutron, a positron, and a neutrino; or, a neutron
218 decays into a proton, an electron and an antineutrino. The weak interaction allows for quark flavor
219 mixing, the which enables beta decay. The W^+ , W^- , and Z^0 are the force carriers of the weak force.
220 The effective range of the weak force is limited to subatomic distances, as a result of the massive
221 nature of the mediator bosons. The unified theory of the electroweak interaction posits that at high
222 enough energies the electromagnetic interaction and the weak force merge into the same force.
223 This threshold is termed the unification energy and calculated to be about 246 GeV [1].

224 The strong force confines quarks into hadron particles, such as protons and neutrons. The
225 strong force also allows for the creation of atomic nuclei by binding protons and neutrons together,
226 and is generally referred to as the “nuclear force” in this context. The gluon is the mediator of
227 the strong force, which is a short-range force which acts at subatomic distances on the order of
228 10^{-15} m. At this range, the strong force is about 100x as strong as the electromagnetic force,
229 which allows for the creation of positively charged nuclei [2]. The strong force is described by the
230 theory of quantum chromodynamics (QCD). In the same way that QED dictates the interaction of
231 electrically charges particles, QCD dictates the interactions of *color-charged* particles. Due to the
232 particular importance of QCD in this thesis, this topic will be explored in detail in section 1.2.

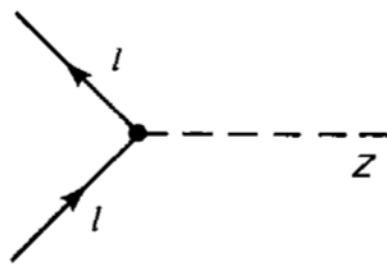
233 The fundamental Feynmann diagram for each of the three forces discussed here is depicted
234 in Figure 1.2. The fourth fundamental force, gravity, is not currently explained by any known
235 mechanism within the Standard Model.



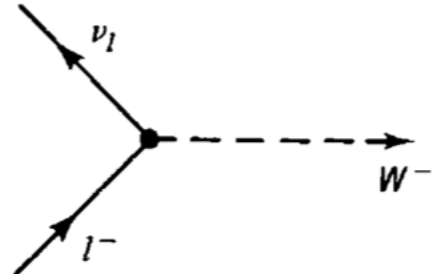
(a) The electromagnetic force



(b) The strong force



(c) The neutral weak force



(d) The charged weak force

Figure 1.2: Fundamental particle interactions of the three fundamental forces described by the Standard Model [2].

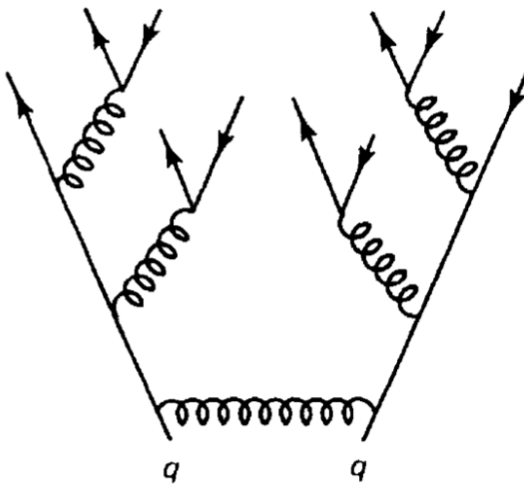


Figure 1.3: An example Feynmann diagram of jet production

236 1.2 QCD and Jets

237 While there is only one type of electric charge, there are three types of color charge; red, green,
238 and blue. In the process $q \rightarrow q + g$, the color of the quark can change. In order to conserve color
239 charge, gluons are bicolored, and always carry some positive color charge and some negative color
240 charge.

241 Color charged particles can only exist in bound states which result in a neutral total color
242 charge, a principle known as confinement. This requires that quarks and gluons exist in group
243 states known as hadrons; either mesons in the case of two quarks or baryons in the case of three
244 quarks. When a quark is separated from a hadron, confinement dictates that other colored objects
245 are produced around the quark to obey confinement. An example of this process is shown in
246 Figure 1.3. This ensemble of objects, generally a mixture of quarks and gluons, is termed a *jet*.
247 Jets are among the most common phenomenon observed by detectors at hadron colliders, and their
248 complex structure makes them a key focus of many physics analyses.

249 **1.3 Symmetries**

250 The Standard Model is a renormalizable quantum field theory that obeys the local symmetry

251 G_{SM} :

$$G_{SM} = SU(3)_C \times SU(2)_L \times U(1)_Y. \quad (1.1)$$

252 The $SU(3)_C$ symmetry component represents the non-Abelian gauge group of QCD. There
253 are 8 generators for the $SU_C(3)$ group which correspond to 8 types of gluon, each representing a
254 different superposition of color charge [3]. The $SU(2)_L \times U(1)_Y$ symmetry group represents the
255 electroweak sector of the Standard Model, which can be spontaneously broken into the electromag-
256 netic and weak sectors. There are 4 generators for this group, which correspond to four massless
257 gauge bosons W^1 , W^2 , W^3 , and B . From these massless gauge bosons are formed the massive
258 mediators of the weak force, the W^- , W^+ and Z^0 bosons, and the massless electromagnetic force
259 carrier, the photon γ . Spontaneous symmetry breaking and the process by which gauge bosons
260 acquire mass will be addressed in section 1.3.1.

261 Noether's theorem [4] stipulates that any continuous symmetry is associated with a conserved
262 quantity. In the Standard Model, this means that the $SU(3)_C$ symmetry gives rise to conservation of
263 color charge. The $SU(2)_L \times U(1)_Y$ symmetry gives rise to conservation of electromagnetic charge.
264 Conservation of spin results from the Poincaré symmetry described by the theory of special rela-
265 tivity, which combined with Noether's theorem gives us the conversation of energy, momentum,
266 and angular momentum.

267 The SM Lagrangian is invariant under CPT symmetry, or charge, parity, and time reversal.
268 Charge conjugation (C) transform a particle into it's corresponding antiparticle by reversing the
269 charge and other quantum numbers. Parity conjugation (P) reverses spatial coordinates, which
270 transforms left-handed particles into right-handed particles and vice-versa. Time reversal (T) is
271 the theoretical process of reversing time. The L subscript in the $SU(2)_L$ group indicates that this
272 symmetry only applies to left-handed fermions. As a result, the $W^{1,2,3}$ gauge bosons of $SU(2)_L$

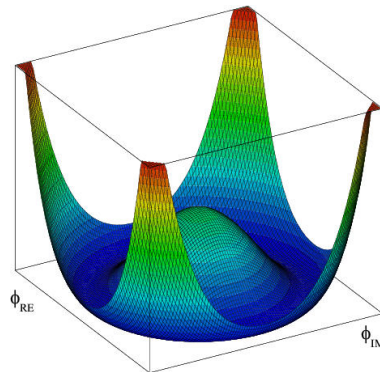


Figure 1.4: An illustration of the “hat shaped” potential of the Higgs field, resulting in a non-zero vacuum expectation value.

273 only interact with left handed particles, a process which maximally violates P-symmetry in the
274 weak force. A small amount of the CP symmetry violation is also observed in the Standard Model,
275 through the decays of strange flavored mesons [5]. The CPT theorem posits that the violation of
276 CP symmetry implies that T-symmetry must also be violated, so that CPT is a preserved symmetry.

277 1.3.1 Spontaneous Symmetry Breaking and The Higgs Mechanism

278 Spontaneous symmetry breaking is the process by which a Lagrangian obeys a symmetry at
279 high energies, but exhibits asymmetric behavior at lower energies. The electroweak symmetry
280 group is spontaneously broken as $SU(2)_L \times U(1)_Y \rightarrow U(1)_{EM}$. The quantity conserved by the
281 $SU(2)_L$ symmetry is weak isospin $T_{1,2,3}$, while the quantity conserved by $U(1)_Y$ symmetry is weak
282 hypercharge Y . Below very high energies, the presence of the Higgs field causes the electroweak
283 symmetry to break. The Higgs field is scalar field which forms a complex doublet of the $SU(2)$
284 symmetry group, with four degrees of freedom. The shape of the Higgs field potential, shown in
285 Figure 1.4, results in a ground state with a non-zero vacuum expectation value; thus the Higgs field
286 takes a non-zero value throughout all space, which breaks the symmetry of the weak isospin $SU(2)$
287 group.

288 The interaction with the Higgs field mixes the four massless gauge bosons $W^{1,2,3}$ and B . Three
289 Higgs field degrees of freedom mix with the massless gauge bosons, resulting in three massive
290 gauge bosons W^- , W^+ and Z^0 . The massless photon γ is created from the components of the

291 massless gauge bosons which do not interact with the Higgs field. The scalar Higgs boson arises
292 from the one unmixed degree of freedom the Higgs field. Spontaneous symmetry breaking also
293 violates the conservation of weak isospin and weak hypercharge, leaving only electromagnetic
294 charge ($Q = T_3 + \frac{1}{2}Y$) as a conserved quantity associated with the $U(1)_{EM}$ symmetry.

295 **1.4 Experimental Validation of the Standard Model**

296 The theoretical framework of the Standard Model coalesced into a unified theory in the mid-
297 20th century. A cascade of discoveries providing empirical evidence for the model followed
298 closely. In the 1960s, three quarks (up, down and strange) and four leptons (electron, muon,
299 and their associated neutrinos) were the known particulate building blocks of matter and the Stan-
300 dard Model. The discovery of the charm quark in 1974, through the observation of the J/ψ meson
301 [6][7], confirmed the existence of a fourth quark flavor. The discovery of the τ in 1975 [8] provided
302 the first evidence of a 3rd generation of matter. This was quickly followed by the observation of
303 the Υ meson in 1977 [9], which provided evidence for the existence of a fifth quark, the b quark
304 (bottom, or beauty). The existence of a 3rd generation of fermion also explained the observation
305 of CP violation in the weak force, as it allowed for the addition of a complex phase in the CKM
306 matrix (a unitary matrix which describes flavor mixing in the weak interaction). The top quark
307 (t) and tau neutrino (ν_τ) were predicted at this point as the final building blocks of three complete
308 generations of fermions, and they were discovered by experimental observation around the turn of
309 the 21st century [10] [11] [12].

310 The W and Z bosons were predicted by the Standard Model, but to observe them required the
311 construction of a particle accelerator powerful enough to produce them. They were finally observed
312 at CERN in 1983 by the UA1 and UA2 experiments [13] [14] at the newly constructed Super Proton
313 Synchrotron (SPS). Their masses were observed to be compatible with the masses predicted by the
314 Standard Model nearly a decade earlier. The final missing piece then was confirming the existence
315 of the Higgs, which again required the construction of a newer and more powerful collider. CERN
316 achieved this with the construction of the Large Hadron Collider (LHC), and in 2012 the ATLAS

317 and CMS experiments announced the discovery of the Higgs particle [15] [16].

318 **1.5 Limitations of the Standard Model**

319 While the Standard Model has enjoyed decades of experimental results which confirm its pre-
320 dictions, there are several glaring shortcomings. The observed phenomenon for which the Standard
321 Model provides no explanation are summarized below.

- 322 • Gravity - the Standard Model does not account for the fourth fundamental force of gravity.
- 323 • Dark Matter - there is no viable candidate to explain the existence of dark matter, a non-
324 interacting form of matter which must exist to account for gravitational observations which
325 cannot be explained by general relativity, such as the motion of galaxies, gravitational lens-
326 ing, and the structure of the universe [17].
- 327 • Matter-Antimatter asymmetry - the level of CP violation in the Standard Model isn't suf-
328 ficient to explain the large discrepancy between the amount of matter and the amount of
329 antimatter in the universe today, and the origins of this imbalance are not understood.
- 330 • Neutrino masses - the Standard Model assumes that neutrinos are massless and provides
331 no mechanism for them to acquire mass. However, observations of neutrino oscillations
332 indicates they posses some small non-zero mass [18].

333 In addition to these unexplained natural phenomenon, there are several questions about the
334 *naturalness* of the Standard Model. The principle of naturalness states that dimensionless ratios
335 between physical constants should be of order 1, and that nature should not be arbitrarily fine-
336 tuned. While this is largely an aesthetic argument, it points to many aspects of the Standard Model
337 for which there exists no natural explanation.

- 338 • Strong CP - while CP symmetry is violated in the weak force, observations indicate that it
339 is preserved by the strong force [19]. The Standard Model predicts that CP violation in the

340 strong force is possible. There is no principle which motivates this incongruity between the
341 weak force and strong force.

- 342 • Hierarchy Problem - The wide range of masses for elementary particles and the wide range of
343 scales at which the four fundamental forces operate is not motivated by the SM. Specifically,
344 it is not understood why the Higgs mass is observed to be well below the Plank scale λ ,
345 which is the energy level at which the effects of quantum gravity become significant. QFT
346 indicates that the Higgs mass is determined by contributions from all energy scales including
347 λ , meaning that its observed mass is inexplicably small.

348 The limitations of the Standard Model provide a road map for theoretical and experimental
349 particle physicists, who seek to develop new theories which account for these observations, and
350 then to find evidence which might support these *Beyond the Standard Model* (BSM) theories. The
351 next chapter will introduce the BSM theories which motivate the physics search presented in this
352 thesis.

353

354

Chapter 2: Physics Beyond the Standard Model

355 In light of the various phenomenon unexplained by the Standard Model, physicists have pro-
356 posed various extensions to the Standard Model, collectively termed *Beyond the Standard Model*
357 (BSM) theories. A particular focus of the physics programs at the Large Hadron Collider (LHC) are
358 BSM models which suggest dark matter candidate particles. If these particles couple to Standard
359 Model, they could be produced and observed at the LHC.

360 **2.1 Hidden Valley Models**

361 Hidden Valley (HV) models are a category of BSM models that allow for dark matter (DM)
362 production at the LHC. They extend the Standard Model with an additional non-Abelian gauge
363 group [20]. This introduces the possibility of a complex dark sector, which mirrors the complexities
364 of Standard Model QCD, and introduces the possibility of dark quarks and gluons. The term
365 “hidden valley” refers to the idea that the DM is hidden from the SM by a high-energy barrier, as
366 illustrated in Figure ???. The dark sector is assumed to communicate with the Standard Model via
367 a “portal”, or “messenger particle”, that can interact with both Standard Model and HV forces. For
368 the s-channel scenario, the portal is considered to be a new massive mediator particle Z' .

369 The portal particle allows for the production of dark sector particles at hadron colliders. If
370 dark quarks are produced via the decay $Z' \rightarrow q_D q_D$ they can hadronize and form dark jets. The
371 properties of the dark jets are determined by the dynamics of the dark sector, which are explored in
372 the subsequent section. Depending on the details of the model, the jets formed by the dark hadrons
373 can be categorized as fully dark, semi-visible, leptonic, emerging, or other [20].

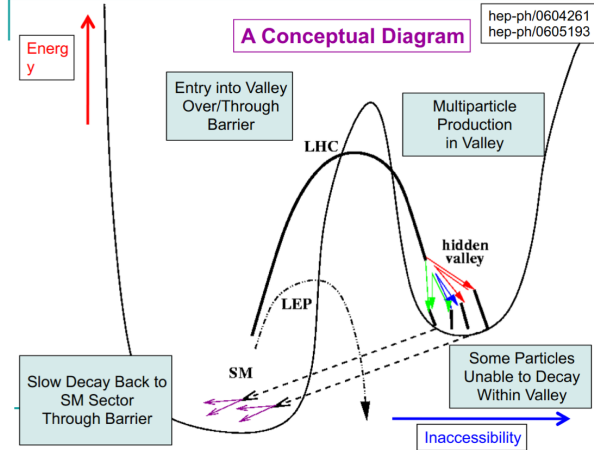


Figure 2.1: Illustration of the hidden valley potential

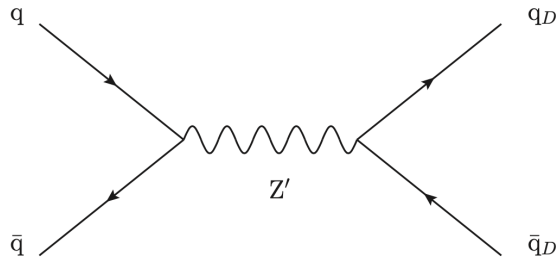


Figure 2.2: The massive mediator particle Z' of the s-channel realization of a HV model

³⁷⁴ 2.2 Dark QCD

³⁷⁵ The theoretical underpinning of the semi-visible jet phenomenology is a dark sector with a
³⁷⁶ gauge group $SU(N_d)$ leading to confinement at a scale Λ_d . For illustration, let's consider the
³⁷⁷ case of an $SU(2)_d$ gauge theory, which gives rise to two dark fermionic generations $\chi_a = \chi_1, \chi_2$.
³⁷⁸ Following the work of Timothy Cohen, et.al. we can write the fundamental dark Lagrangian as:

$$\mathcal{L}_{dark} \supset -\frac{1}{2} \text{Tr } G_{\mu\nu}^d G^{d\mu\nu} - \bar{\chi}_a (i \not{D} - M_{d,a}) \chi_a \quad (2.1)$$

³⁷⁹ The first term allows for the dark gluons to self-interact, while the second term enables the dark
³⁸⁰ quarks to hadronize and acquire mass. The dark quarks are assumed to have a common mass M_d .
³⁸¹ The coupling strength of the strongly interacting dark quarks is termed α_d . At the confinement

382 scale Λ_d , the dark quarks can form bound states. At the scale $M_d \approx \Lambda_d$ a QCD-like show occurs.

383 The properties of the hadrons formed by the dark quarks are of particular importance to the
384 observed dark QCD dynamics. Dark-isospin number $U(1)_{1-2}$ and dark-baryon number $U(1)_{1+2}$
385 are accidental symmetries of the theory which determine the stability of the hadrons. In the case
386 of two dark flavors, six dark hadrons can be formed: four mesons ($\chi_1\bar{\chi}_1$, $\chi_2\bar{\chi}_2$, $\chi_1\bar{\chi}_2$, $\bar{\chi}_1\chi_2$) and
387 two baryons ($\bar{\chi}_1\bar{\chi}_2$, $\bar{\chi}_1\bar{\chi}_2$). The mesons $\chi_1\bar{\chi}_2$ and $\bar{\chi}_1\chi_2$ are charged under dark-isospin and will be
388 stable if this symmetry is unbroken. The baryons would also be stable as they are charged under
389 the dark-baryon number. These four stable hadrons become dark matter candidates of the theory.
390 The $\chi_1\bar{\chi}_1$ and $\chi_2\bar{\chi}_2$ mesons are not charged under either symmetry and are thus expected to decay.
391 The unstable mesons can decay into stable dark mesons, or into an off-shell Z' . The off-shell Z'
392 will then decay into two DM quarks or two SM quarks, and its products will continue to shower
393 until the final state particles are stable.

394 The number of stable and unstable dark states varies substantially depending on the details
395 of the model. The model discussed above can be generalized from $SU(2)_d$ to $SU(N)_d$, with any
396 number of colors N_c or flavors N_f . This affects the ratio of possible stable to unstable mesons,
397 which can directly impact the amount of missing energy. The fraction of missing energy is a
398 variable in many dark QCD models, and is especially important in the case of semi-visible jets.

399 2.3 Semi-visible Jets

400 A “semi-visible jet” occurs when the heavy Z' messenger particle decays into dark quarks,
401 which then hadronize in a QCD-like shower. If some of the dark hadrons are stable while others
402 decay to SM quarks via the off-shell Z' , a collimated mixture of visible and dark matter is formed
403 – this is termed a semi-visible jet. If the Z' messenger particle is produced at rest, the two jets will
404 be back-to-back in the transverse plane. If there is an imbalance in the amount of invisible particles
405 between the two jets, one of the jets will be observed to be aligned with missing transverse energy.

406 While there are a myriad of HV and dark QCD models, a handful of model parameters are most
407 important in determining the observable of these showers within a particle detector. The coupling

408 strength α_d is one of the most important, as it controls the fraction of dark hadrons emitted in the
409 shower and their average p_T . The mass of the dark quarks directly impacts the jet mass. If the
410 masses of the dark quark flavors are comparable, the ratio of stable to unstable dark hadrons will
411 be approximately 1:1. However, if there is a mass splitting, stable or unstable dark hadrons may
412 be favored, which impacts the amount of missing energy observed.

413 The ratio of stable to unstable dark hadrons in the shower is a critical variable for capturing the
414 behavior of dark showers. This value is termed r_{inv} :

$$r_{inv} = \frac{\# \text{ of stable hadrons}}{\# \text{ of hadrons}} \quad (2.2)$$

415 Events containing jets aligned with missing transverse momentum are generally considered to
416 be misreconstructed by other DM searches, and therefore discarded. This class of final states is
417 therefore largely uncovered by existing DM searches. The nature of the dark hadron shower is
418 determined by the following parameters: the Z' mass $m_{Z'}$, the Z' couplings to visible and dark
419 quarks g_q and g_{q_D} , the number of dark colors and flavors, the characteristic scale of the dark sector
420 confinement Λ_D , the scale of the dark hadrons m_D , and the average fraction of stable hadrons in
421 the decay r_{inv} . The coupling to SM quarks determines the Z' production cross section.

422

Part II

423

Experiment

424

425

Chapter 3: The Large Hadron Collider

426 The Large Hadron Collider (LHC) is a 26.7 km circular high-energy particle accelerator, span-
427 ning the Swiss-French border near the city of Geneva, Switzerland [21]. The LHC occupies the
428 tunnel constructed in 1989 for the Large Electron-Positron (LEP) Collider, and reaches a maxi-
429 mum depth of 170m below the surface. The LHC is operated by the European Organization for
430 Nuclear Research (CERN), the largest international scientific collaboration in the world.

431 The LHC accelerates protons and heavy ions, and collides them at four interaction points
432 around the ring, with a design center-of-mass energy per collision of $\sqrt{s} = 14$ TeV. Each interaction
433 point is home to one of four detector experiments, which study the products of the collisions. The
434 largest of these experiments is the ATLAS detector, a general purpose detector designed to study
435 the Standard Model and search for new physics that could be produced in LHC collisions [22].
436 The CMS detector is another general purpose detector, designed and operated independently of the
437 ATLAS detector, but intended to probe the same range of physics [23]. The ALICE experiment is
438 a dedicated heavy ion experiment, and the LHC-b experiment is a dedicated *b*-physics experiment
439 [24] [25].

440 This chapter will cover the multi-component accelerator complex powering the LHC, the state-
441 of-the-art magnets which steer the particle beams, measurements of the intensity and number of
442 collisions produced by the LHC, and finally an overview of LHC activities in the past, present, and
443 future.

444 **3.1 Accelerator Physics**

445 **3.1.1 The Journey of a Proton**

446 From 2010 - 2018, the protons which fed the LHC started as hydrogen gas. The electrons were
447 removed from the hydrogen atoms through the use of strong electric fields. The linear accelerator
448 LINAC2 then accelerated the protons to an energy of 50 MeV. Between 2018 and 2020, LINAC2
449 was replaced with LINAC4, which instead accelerates H^- ions, hydrogen atoms with two electrons.
450 LINAC4 is capable of accelerating the H^- ions to 160 MeV. Before injection to the next part of
451 the acceleration chain, both electrons are stripped from the H^- ions, leaving just protons. From
452 here the protons enter the Proton Synchrotron booster, where they are accelerated up to 1.4 GeV of
453 energy. Subsequently they are sorted into bunches separated in time by 25 ns, where each bunch
454 contains approximately 10^{11} protons. Next the bunches pass through the Proton Synchrotron (PS)
455 and the Super Proton Synchrotron (SPS), where they reach energies of 25 GeV and 450 GeV
456 respectively. Finally they are injected into the LHC as two beams traveling in opposite direction.
457 The original design allowed each beam to be accelerated up to 7 TeV of energy. Due to limitations
458 in the performance of the superconducting LHC magnets, the highest energy actually achieved by
459 the LHC beams during Run 2 was 6.5 TeV, giving a collision center-of-mass energy of $\sqrt{s} = 13$
460 TeV [26]. Figure 3.1 shows the full LHC accelerator complex.

461 Acceleration in the LHC is performed by eight radio frequency (RF) cavities located around the
462 ring. Each RF cavity produces a 2 MV electric field oscillating at 40 MHz. The 40MHz oscillation
463 produces a point of stable equilibrium every 2.5 ns. These points of equilibrium are synchronized
464 with the occurrence of the proton bunches produced in the PS – a proton bunch occupies one out
465 of every ten points of stable equilibrium, such that the bunches maintain a 25 ns spacing [26].

466

The CERN accelerator complex Complexe des accélérateurs du CERN

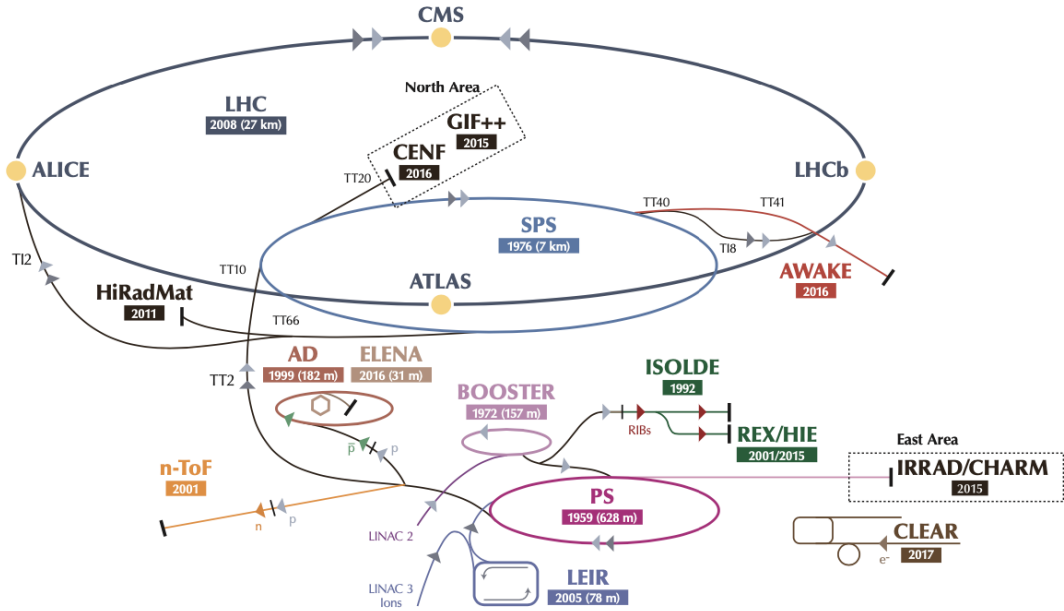


Figure 3.1: The LHC accelerator complex at CERN [27]

467 3.1.2 Magnets

468 In addition to the acceleration cavities, the LHC houses 9593 superconducting magnets which
 469 direct and focus the proton beam on its 27 kilometer journey. The magnets are comprised of super-
 470 conducting Niobium-Titanium coils cooled to 1.9K by superfluid helium. As the beams approach
 471 one of the four collision points around the ring, multipole magnets focus and squeeze the beam for
 472 optimal collisions [26].

473 The LHC is divided into sections, where each section contains an arc and a straight insertion. The arcs are composed of 1232 large dipole magnets which bend the beam
 474 to follow the roughly circular 27 km path. The main dipoles generate powerful 8.3 tesla magnetic
 475 fields to achieve this bend. Each dipole magnet is 15 meters long and weighs 35 tonnes. The
 476 dipoles work in conjunction with quadrupole magnets, which keep the particles in a focused beam,
 477 and smaller sextupole, octupole and decapole magnets which tune the magnetic field at the ends of
 478 the dipole magnets [28].

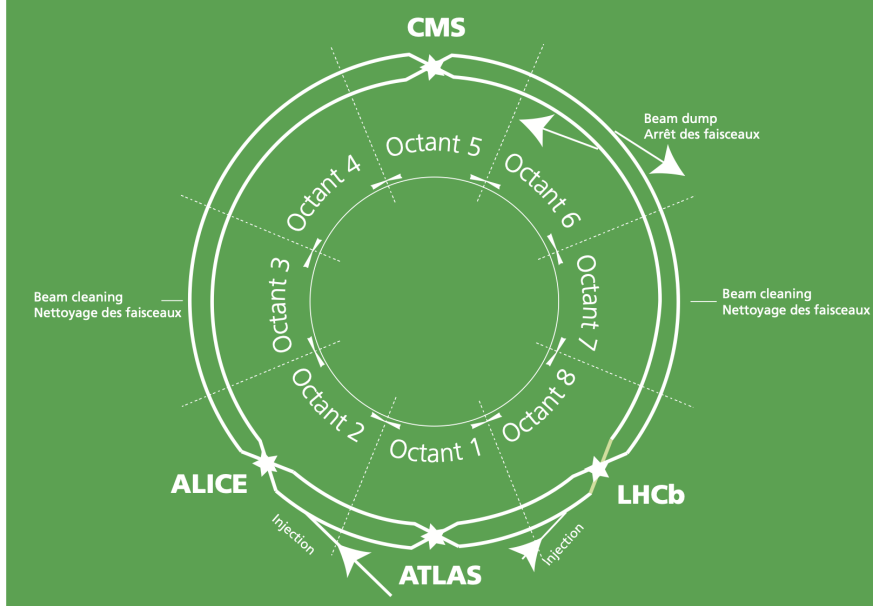


Figure 3.2: The octants of the LHC and location of various beam activities [26]. Stars indicate the locations of beam collisions, and the associated detectors recording the outcome of those collisions.

480 The straight insertion sections have different purposes depending on their location around the
 481 ring: beam collisions, beam injection, beam dumping, or beam cleaning. At the four collision
 482 points, insertion magnets squeeze the beam to ensure a highly focused collision. This is accom-
 483 plished with a triplet of quadrupole magnets, which tighten the beam from 0.2 millimeters to just
 484 16 micrometers in diameter. Insertion magnets also clean the beam, which prevents stray particles
 485 from hitting sensitive components throughout the LHC. When the LHC is ready to dispose of a
 486 beam of particles, beam dump magnets deflect the path of the beam into a straight line towards
 487 a block of concrete and graphite that stops the beam. A dilution magnet then reduces the beam
 488 intensity by a factor of 100,000 before the final stop [28]. Figure 3.2 shows the locations various
 489 beam activities.

490 **3.2 Luminosity**

491 Collisions at the LHC occur when the two beams of proton bunches cross at one of the four
 492 interaction points. The intensity of collisions is described by the instantaneous luminosity, the

493 formula for which is given in equation 3.1.

$$L = \frac{fN_1N_2}{4\pi\sigma_x\sigma_y} \quad (3.1)$$

494 Here f is the revolution frequency, N_1 and N_2 are the number of particle per bunch for each
495 beam, and σ_x , σ_y are the horizontal and vertical beam widths.

496 The instantaneous luminosity gives the number of the collisions that could be produced at the
497 interaction point per unit of cross-sectional area per unit of time, generally expressed in $\text{cm}^{-2}\text{s}^{-1}$.
498 The integrated luminosity is obtained by integrating the instantaneous luminosity over a given
499 block of time, and measures the total number of collisions which have occurred during that op-
500 eration period. The total integrated luminosity is directly correlated with the size of the datasets
501 collected by the LHC experiments. Total integrated luminosity for Run 2 is illustrated in Figure
502 3.3.

503 High levels of instantaneous luminosity result in multiple pp collisions per bunch crossing,
504 which leads to an effect known as *pileup*. Pileup poses a challenge for detector physics, as recon-
505 structing the products of multiple simultaneous events is far more challenging than reconstructing
506 a single event with no pileup. Pileup conditions vary from year-to-year and run-to-run of LHC op-
507 eration, and the impact of these conditions are taken into account when analyzing the data, as will
508 be discussed further in Chapter 5. Measurement of pileup conditions during Run 2 are illustrated
509 in Figure 3.3.

510 The design peak luminosity of the LHC is $1.0 \times 10^{34} \text{ cm}^{-2}\text{s}^{-1}$. During Run 1 of the LHC the
511 peak instantaneous luminosity was $0.8 \times 10^{34} \text{ cm}^{-2}\text{s}^{-1}$. Over the course of Run 1 the LHC collected
512 a total integrated luminosity of 5.46 fb^{-1} at $\sqrt{s} = 7 \text{ TeV}$, and 22.8 fb^{-1} at $\sqrt{s} = 8 \text{ TeV}$. Following the
513 first long shutdown and upgrade phase of operations, the LHC achieved a center of mass energy
514 $\sqrt{s} = 13 \text{ TeV}$ at the beginning of Run 2 in 2015. The LHC was also able to deliver 2.0×10^{34}
515 $\text{cm}^{-2}\text{s}^{-1}$ peak instantaneous luminosity, double the design value. During LHC Run 2, from 2015-
516 2018, the LHC delivered 156 fb^{-1} of integrated luminosity for proton-proton collisions. Run 3 of

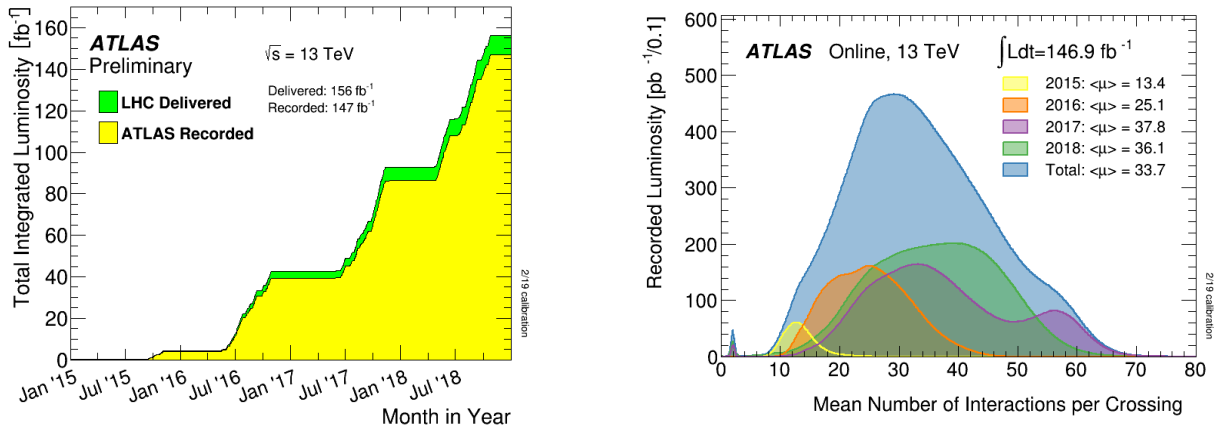


Figure 3.3: (Left) Total integrated luminosity over the course of Run 2. (Right) Average number of pp interactions per bunch crossing in Run 2. Each curve is weighted by the integrated luminosity for the year.

517 the LHC began in 2022, and is expected to deliver 250 fb^{-1} of integrated luminosity to the ATLAS
518 and CMS experiments by 2026 [29].

519 The goal of LHC physic analyses is to find and study rare events produced by interesting
520 physics processes. The cross section σ of a given process indicates the probability of that process
521 occurring given the beam conditions of the LHC. Multiplying the cross section by the integrated
522 luminosity of a dataset gives the expected number of events for that process within the dataset.

$$N_{\text{events}} = \int \sigma L(t) dt = \mathcal{L} \times \sigma \quad (3.2)$$

523 The cross section for most processes of interest, especially BSM processes, is several orders of
524 magnitude below the total cross section for the LHC. Therefore maximizing the number of events
525 produced in collisions is crucial to increase the likelihood of producing events from processes of
526 interest. For this reason, maximizing instantaneous luminosity is a key factor in accelerator design
527 and operation, while mitigating the resulting pileup effects is a key component in detector design
528 and operation.

529 **3.3 LHC Timeline**

530 The first proton-proton collisions at the LHC were achieved in 2010 with a center-of-mass
531 energy of $\sqrt{s} = 7$ TeV. Run 1 of the LHC took place between 2010 and early 2013, during which
532 time the center-of-mass collision energy increased from 7 TeV to 8 TeV. Figure 3.4 shows an
533 overview of LHC activities beginning in 2011, in the midst of Run 1. The data collected during
534 Run 1 led to the discovery of the Higgs Boston in 2012 [30].

535 Between 2013 and 2015 the LHC underwent the first Long Shutdown (LS1) during which
536 time maintenance and renovation was performed on the accelerator chain, including the repair and
537 consolidation of the high-current splices which connect the super-conducting LHC magnets. Run
538 2 of the LHC took place from 2015 to 2018 and achieved a center-of-mass energy of $\sqrt{s} = 13$ TeV.
539 Analysis of data collected in Run 2 is still on going, and is the subject of study in this thesis.

540 Between 2018 and 2022 the LHC underwent the second Long Shutdown (LS2), allowing for
541 further detector and accelerator maintenance and upgrades. Key improvements to the LHC in-
542 cluded the improvement of the insulation for over 1200 diode magnets, and the upgrade from
543 LINAC2 to LINAC4 mentioned in Section 3.1.1. Run 3 of the LHC began in 2022 and achieved a
544 center-of-mass energy of $\sqrt{s} = 13.6$ TeV.

545 Run 3 is scheduled to continue through 2026, at which point the LHC machine and detectors
546 will undergo upgrades for the *high luminosity* LHC (HL-LHC). The HL-LHC will increase the
547 instantaneous machine luminosity by a factor of 5 - 7.5 with respect to the nominal LHC design.
548 The bottom panel of Figure 3.4 shows an overview of the preparation work for the HL-LHC that
549 has been going on concurrently with Run 1, 2, and 3 of the LHC [31].



Figure 3.4: Timeline of LHC and HL-LHC activities [29]. Integrated luminosity estimates are approximate, and not reflective of the exact amount delivered to each experiment.

550

551

Chapter 4: The ATLAS Detector

552 The ATLAS detector (**A** Toroidal **L**H**C** Apparatu**S**) is one of two general purpose physics
553 detectors designed to study the products of proton-proton collisions at the LHC. The detector is
554 composed of a variety of specialized subsystems, designed to fully capture a wide array of physics
555 processes. The apparatus is 25m high, 44m in length, and weighs over 7000 tons [32]. The LHC
556 beam pipes direct proton beams to an interaction point at the center of ATLAS, and the cylindrical
557 detector design captures a complete 360° view of the *event*, tracking all particles that result from
558 the collision.

559 The main components of the ATLAS detector are the Inner Detector (ID) which provides high
560 precision tracking of charged particles leaving the collision vertex, the calorimeter system which
561 measures the energy of electromagnetic and hadronic objects, and the Muon Spectrometer (MS)
562 which gives detailed information about muons that reach the outer radii of the detector. Two
563 magnet systems, a 2 T solenoid magnet surrounding the ID, and a 0.5-1.0 T toroid magnet system
564 situated throughout the MS, produce magnetic fields which bend the trajectory of charged particles
565 traversing the detector. In addition to the main detector components, dedicated forward detectors
566 monitor beam conditions and instantaneous luminosity, and an online trigger system reduces the
567 data rate to a manageable level for storage. Each of these components will be discussed in further
568 detail in this chapter.

569 4.1 Coordinate System and Geometry

570 The ATLAS detector employs a right hand cylindrical coordinate system. The z axis is aligned
571 with the beam line, and the x-y plane sits perpendicular to the beam line. The coordinate system
572 origin is centered on the detector, such that the origin corresponds with the interaction point of the

573 two colliding beams. The detector geometry is usually characterized by polar coordinates, where
574 the azimuthal angle ϕ spans the x-y plane. The polar angle θ represents the angle away from the
575 beam line, or z axis. $\theta = 0$ aligns with the positive z -axis, and $\phi = 0$ aligns with the positive x-axis.

576 The polar coordinate θ is generally replaced by the Lorentz invariant quantity *rapidity* or y :

$$y = \frac{1}{2} \ln\left(\frac{E + p_z}{E - p_z}\right). \quad (4.1)$$

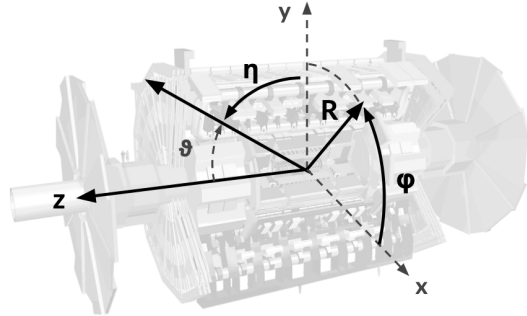
577 This substitution is advantageous because objects in the detector are traveling at highly rela-
578 tivistic speeds. The relativistic speed also means that the masses of the particles are generally small
579 compared to their total energy. In the limit of zero mass, the rapidity y reduces to the pseudorapid-
580 ity η , which can be calculated directly from the polar angle θ :

$$\eta = -\ln\left(\frac{\theta}{2}\right). \quad (4.2)$$

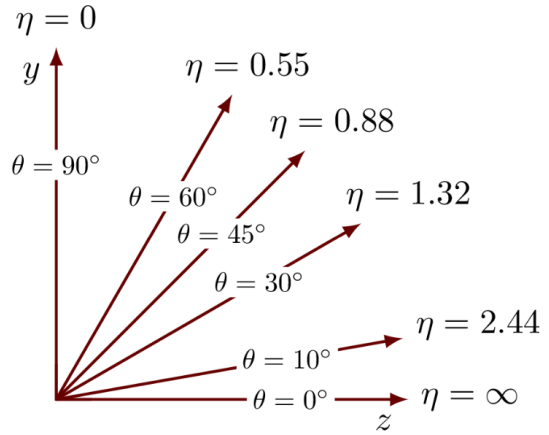
581 The distance between physics objects in the detector is generally expressed in terms of the solid
582 angle between them ΔR :

$$\Delta R = \sqrt{\Delta\phi^2 + \Delta\eta^2} \quad (4.3)$$

583 Figure 4.1a depicts the orientation of the coordinate system with respect to the ATLAS detector,
584 while Figure 4.1b illustrates the relationship between θ , η , and the beamline axis z . Direct or “head
585 on” proton-proton collisions are more likely to result in objects whose momentum is directed
586 along transverse plane (low $|\eta|$); glancing proton-proton collisions are more likely to result in
587 objects whose momentum is directed along the z -axis (high $|\eta|$). Due to the difference in the
588 nature of these collisions, as well as the cylindrical design of the ATLAS detector, the detector
589 is divided into regions of low and high η . Each subsystem has a “central” or “barrel” region
590 covering low $|\eta|$, while the “forward” or “end-cap” regions cover the area up to $|\eta| = 4.9$. Each of
591 the three main ATLAS subsystems will be discussed in the following sections.



(a) The ATLAS geometry



(b) Relationship between η and θ

Figure 4.1: ATLAS coordinate system and geometry

592 4.2 Inner Detector

593 The Inner Detector (ID) is the ATLAS subsystem closest to the interaction point. The primary
 594 purpose of the ID is to determine the charge, momentum, and trajectory of charged particles pass-
 595 ing through the detector. With this information the ID is also able to precisely determine interaction
 596 vertices.

597 The ID is composed of three sub-detectors; the Pixel Detector, the Semiconductor Tracker
 598 (SCT) and the Transition Radiation Tracker (TRT). Figure 4.2 shows the location of these three
 599 subsystems with respect to each other and the interaction point.

600 4.2.1 Pixel Detector

601 The pixel detector is the first detector encountered by particles produced in LHC collisions.
 602 The original pixel detector consists of 3 barrel layers of silicon pixels, positioned at 5 cm, 9 cm
 603 and 12 cm from the beamline. There are also 3 disks on each end-cap positioned 50 - 65 cm from
 604 the interaction point, providing full coverage for $|\eta| < 2.2$. The layers are comprised of silicon
 605 pixels each measuring $50 \times 400 \mu\text{m}^2$, with 140 million pixels in total. The pixels are organized
 606 into modules, which each contain a set of radiation hard readout electronics chips. In 2014, the
 607 Insertable B-layer (IBL) was installed, creating a new innermost layer of the pixel detector sitting

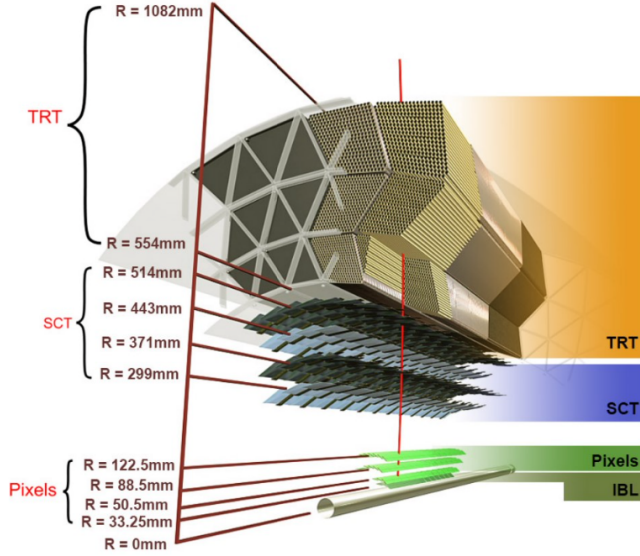


Figure 4.2: A 3D visualization of the structure of the ID in the barrel region [33]

608 just 3.3 cm from the beamline. The pixels of the IBL measure $50 \mu\text{m}$ by $250 \mu\text{m}$, and cover
 609 a pseudo-rapidity range up to $|\eta| < 3$. The IBL upgrade enhances the pixel detector's ability
 610 to reconstruct secondary vertices associated with short-lived particles such as the b-quark. The
 611 improved vertex identification also helped compensate for increasing pile-up in Run 2 [32].

612 4.2.2 Semiconductor Tracker

613 The SCT provides at least 4 additional measurements of each charged particle. It employs the
 614 same silicon technology as the Pixel Detector, but utilizes larger silicon strips which measure $80 \mu\text{m}$
 615 by 12.4 cm . The SCT is composed of 4 barrel layers, located between 30 cm and 52 cm from
 616 the beamline, and 9 end-cap layers on each side. The SCT can distinguish tracks that are separated
 617 by at least $200 \mu\text{m}$.

618 4.2.3 Transition Radiation Tracker

619 The TRT provides an additional 36 hits per particle track. The detector relies on gas filled
 620 straw tubes, a technology which is intrinsically radiation hard. The straws which are each 4 mm in
 621 diameter and up to 150 cm in length and filled with xenon gas. The detector is composed of about

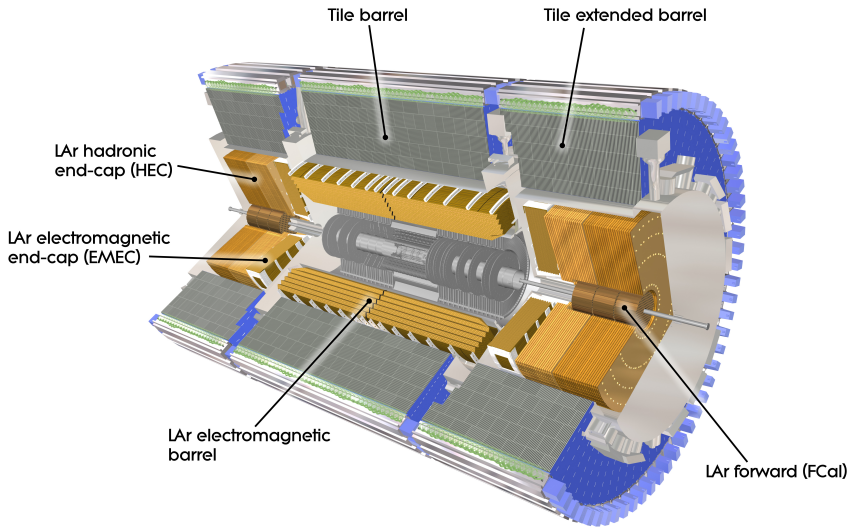


Figure 4.3: ATLAS calorimetry system [34]

622 50000 barrel region straws and 640000 end-cap straws, comprising 420000 electronic readout
 623 channels. Each channel provides a drift time measurement with a spatial resolution of $170\text{ }\mu\text{m}$ per
 624 straw. As charged particles pass through the many layers of the detector, transition radiation is
 625 emitted. The use of two different drift time thresholds allows the detector to distinguish between
 626 tracking hits and transition radiation hits.

627 4.3 Calorimeters

628 The ATLAS calorimeter system is responsible for measuring the energy of electromagnetically
 629 interacting and hadronically interacting particles passing through the detector. The calorimeters are
 630 located just outside the central solenoid magnet, which encloses the inner detectors. The calorime-
 631 ters also stop most known particles, which the exception of muons and neutrinos, preventing them
 632 from traveling to the outermost layers of the detector. The ATLAS calorimetry system is composed
 633 of two subsystems - the Liquid Argon (LAr) calorimeter for electromagnetic calorimetry and the
 634 Tile calorimeter for hadronic calorimetry. The full calorimetry system is shown in Figure 4.3.

635 4.3.1 Liquid Argon Calorimeter

636 The LAr calorimeter is a sampling calorimeter designed to trigger on and measure the ener-
637 gies of electromagnetic (EM) particles, as well as hadronic particles in the high η regions. It is
638 divided in several regions, as shown in Figure 4.3. For the region $|\eta| < 1.4$, the electromagnetic
639 barrel (EMB) is responsible for EM calorimetry, and provides high resolution energy, timing,
640 and position measurements for electrons and photons passing through the detector. The elec-
641 tromagnetic endcap (EMEC) provides additional EM calorimetry up to $|\eta| < 3.2$. In the re-
642 gion $1.4 < |\eta| < 3.2$, the hadronic endcap (HEC) provides hadronic calorimetry. For hadronic
643 calorimetry in the region $|\eta| < 1.4$, corresponding to a detector radii > 2.2 m, the less expensive
644 tile calorimeter (discussed in the next section) is used instead. A forward calorimeter (FCAL)
645 extends the hadronic calorimetry coverage up to $3.1 < |\eta| < 4.8$ [35].

646 The LAr calorimeter is composed of liquid argon sandwiched between layers of absorber mate-
647 rial and electrodes. Liquid argon is advantageous as a calorimeter active medium due to its natural
648 abundance and low cost, chemical stability, radiation tolerance, and linear response over a large
649 energy range [36]. The calorimeter is cooled to 87k by three cryostats: one barrel cryostat encom-
650 passing the EMB, and two endcap cryostats. The barrel cryostat also encloses the solenoid which
651 produces the 2T magnetic field for the inner detector. Front-end electronics are housed outside the
652 cryostats and are used to process, temporarily store, and transfer the calorimeter signals.

653 **Electromagnetic Calorimeter**

654 For the electromagnetic calorimeters, the layers of electrodes and absorber materials are ar-
655 ranged in an an accordion shape, as illustrated in Figure 4.4. The accordion shape ensures that
656 each half barrel is continuous in the azimuthal angle, which is a key feature for ensuring consistent
657 high resolution measurements. Liquid argon permeates the space between the lead absorber plates,
658 and a multilayer copper-polymide readout board runs through the center of the liquid argon filled
659 gap.

660 The detection principle for the LAr calorimeter is the current created by electrons which are

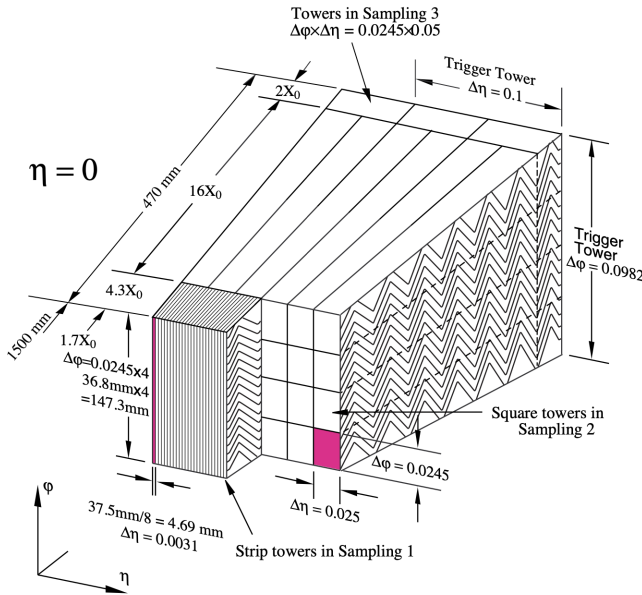


Figure 4.4: Diagram of a segment of the EMB, demonstrating the accordion plate arrangement [35]

released when a charged particle ionizes the liquid argon. In the barrel region, the electrons are driven towards the center electrodes by a 2000 V potential with a drift time of less than 450 ns [37]. In the end-caps the voltage varies as a function of the radius in order to maintain a flat response [35]. The amount of current produced by the ionized electrons is proportional to the energy of the particle creating the signal. Figure 4.5 shows the shape of the signal produced in the LAr calorimeter, before and after it undergoes shaping during the readout process. The shaping of the pulse enforces a positive peak and a negative tail, which ensures that subsequence pulses can be separated with the precision required for the 25 ns LHC bunch spacing [35].

Hadronic End-cap Calorimeter

The HEC sits radially beyond the EMEC. The copper absorber plates in the HEC are oriented perpendicular to the beamline, with LAr as the active medium. Each end-cap is divided into two independent wheels; the inner wheel uses 25 mm copper plates, while the outer wheel uses 50 mm plates as a cost saving measure. In each wheel, the 8.5 mm plate gap is crossed by three parallel

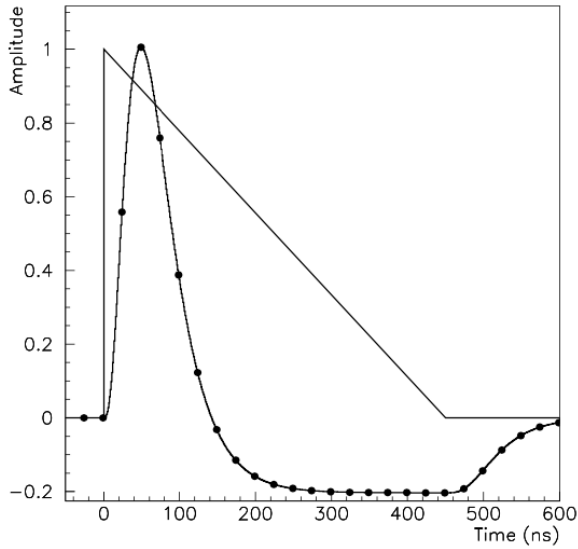


Figure 4.5: A LAr pulse as produced in the detector (triangle) and after shaping (curve) [35]

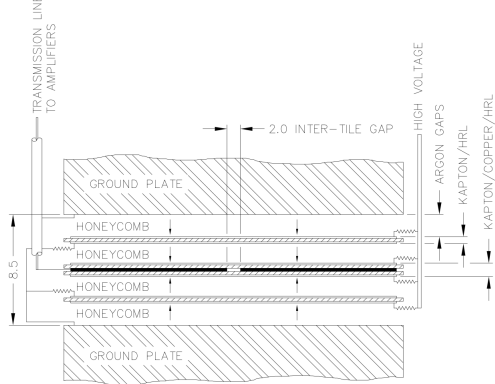


Figure 4.6: Readout gap structure in HEC [35]

674 electrodes, creating an effective drift distance of 1.8 mm. This gap is illustrated in Figure 4.6.
 675 Each wheel is divided into 32 wedge-shaped modules, each containing their own set of readout
 676 electronics.

677 **Forward Calorimeter**

678 The forward range is covered by the FCal, which provides both EM and hadronic calorimetry.
 679 It is composed of three active cylindrical modules; one EM module with copper absorber plates,
 680 and two hadronic modules with tungsten absorber plates. The plates are oriented perpendicular to

681 the beamline, and LAr is used as the active material throughout. The electrodes of the FCal consist
682 of tubes that run parallel to the beam line, arranged in a honeycomb pattern. The resulting LAr
683 gaps are as small as $250\ \mu\text{m}$, which enables the FCal to handle the large influx of particles in the
684 forward region [35].

685 4.3.2 Tile Calorimeter

686 The Tile Calorimeter (TileCal) provides hadronic calorimetry in the region $\eta < 1.7$, and sur-
687 rounds the LAr calorimeter. It is responsible for measurements of jet energy and jet substructure,
688 and also plays an important role in electron isolation and triggering (including muons) [38]. Tile-
689 Cal is composed of 3 sections, as shown in Figure 4.3; a barrel calorimeter sits directly outside the
690 LAr EMB and provides coverage up to $\eta < 1.0$. Two extended barrel sections sit outside the LAr
691 endcaps and cover the region $0.8 < \eta < 1.7$.

692 TileCal is a sampling calorimeter composed of steel and plastic scintillator plates as illustrated
693 in Figure 4.7. A total of 460,000 scintillators are read out by wavelength-shifting fibers. The
694 fibers are gathered to define cells and in turn read out by photomultiplier tubes, which amplify
695 the signal and convert it to an electrical signature. Each cell has an approximate granularity of
696 $\Delta\eta \times \Delta\phi = 0.1 \times 0.1$. Each barrel is divided azimuthally into 64 independent modules, an example
697 of which is show in Figure 4.7. The modules are each serviced by front-end electronic housed in a
698 water-cooled drawer on the exterior of the module.

699 The detection principle of the TileCal is the production of light from hadronic particles inter-
700 acting with the scintillating tiles. When a hadronic particle hits the steel plate, a shower of particles
701 are produced. The interaction of the shower with the plastic scintillator produces photons, the num-
702 ber and intensity of which are proportional to the original particle's energy.

703

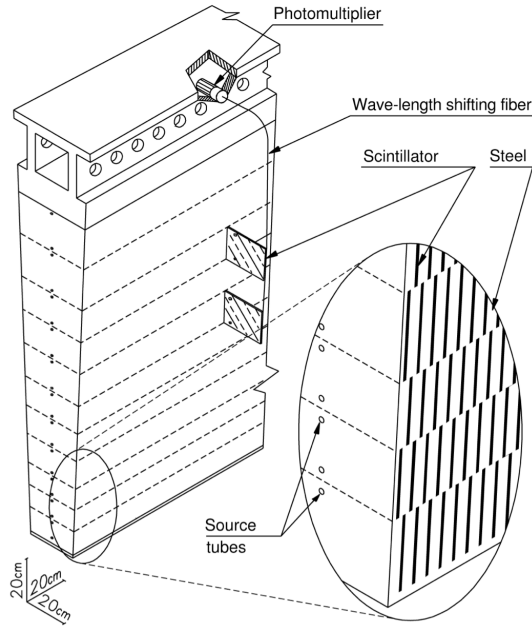


Figure 4.7: TileCal wedge module [38]

704 4.4 Muon Spectrometer

705 Unlike electrons, photons, and hadrons, muons interact minimally with the ATLAS calorimeters,
 706 and can pass through large amounts of detector material without stopping. The ATLAS Muon
 707 Spectrometer (MS) provides additional tracking information to improve the identification and mea-
 708 surement of muons. The MS comprises the outermost layers of the detector, and is interspersed
 709 with toroid magnets (discussed in Section 4.5), which provide a magnetic field of approximately
 710 0.5 T. The magnetic field bends the trajectory of the muons as they pass through the detector, and
 711 the degree of the bend is directly correlated with the muon momentum. The path of the muon is
 712 primarily measured by hits in three layers of Monitored Drift Tube (MDT) precision chambers,
 713 which cover the range $|\eta| < 2.7$. The barrel layout of the MS is show in Figure 4.8.

714 Muon triggering is provided by three layers of Resistive Plate Chambers (RPC) in the barrel
 715 ($|\eta| < 1.05$), and 3 - 4 layers of Thin Gap Chambers (TGC) in the end-caps ($1.05 < |\eta| < 2.4$).
 716 RPCs and TGCs also provide muon track measurements in the non-bending coordinate (ϕ). RPCs
 717 are constructed from two parallel resistive plates separated by a 2mm gap filled with a sensitive

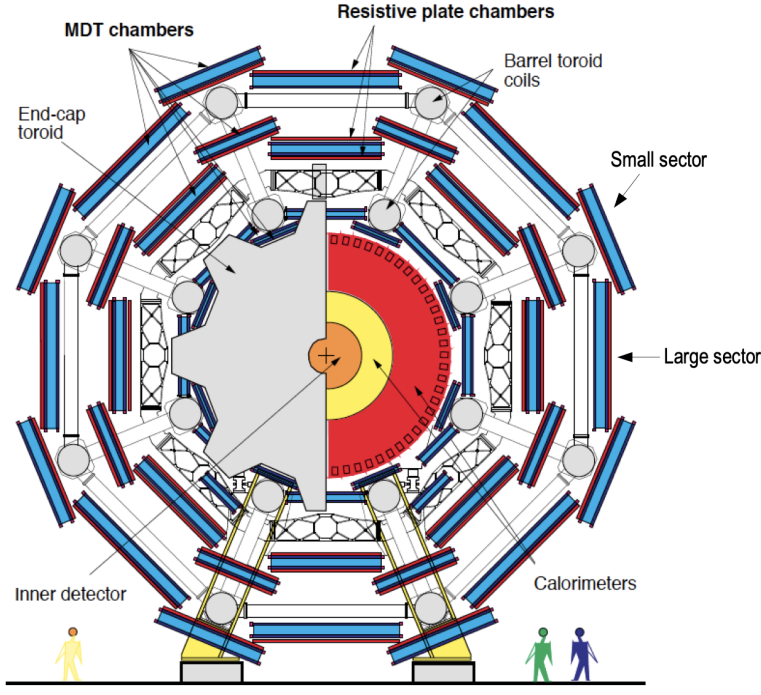


Figure 4.8: Cross section view of the muon spectrometer system [39]

718 gas mixture. This provides a total of six independent measurements for each muon track, with a
 719 spatial resolution of ~ 1 cm and a time resolution of ~ 1 ns. Time measurements from the RPCs
 720 are primarily associated to hits in the MDT precision chambers to determine the bunch crossing.
 721 The time measurement is also used to reject cosmic muons, and to search for delayed signals.
 722 TCGs provide triggering in the end-cap regions, and consist of parallel $30\ \mu\text{m}$ wires suspended
 723 in a sensitive gas mixture. TCGs provide high radiation tolerance and a fast response time, both
 724 features that are necessary for handling the high flux of muons in the forward region [39].

725 Precision measurements of muon momentum and position are primarily achieved by MDTs.
 726 The MDTs are constructed from 30 mm diameter tubes, permeated by a gas mixture of 93% Ar and
 727 7% CO₂. The average single-tube spatial resolution is $80\ \mu\text{m}$. Each chamber consists of six drift
 728 tube layers, which together provide a muon track segment resolution of $35\ \mu\text{m}$. The momentum
 729 of the muons can be calculated from the bend in the muon trajectory as they pass through the
 730 0.5T magnetic field provided by the toroids. For a $p_T = 1$ TeV track, the average p_T resolution is
 731 11%. In the inner most end-cap wheels, Cathode Strip Chambers (CSC) are used instead of MDTs,

732 covering the region $2.0 < |\eta| < 2.7$. CSCs are multi-wire proportional chambers, with a cathode
733 strip readout. The CSCs have a spatial resolution in the range of $50 \mu\text{m}$, and a maximum drift time
734 of about 30 ns, which makes them superior for handling the high flux of particles in the forward
735 region [40].

736 **4.5 Magnet System**

737 The ATLAS magnet system consists of four sets of superconducting magnets: a barrel solenoid,
738 a barrel toroid, and two end-cap toroids. The solenoid magnet produces a 2T magnetic field re-
739 sponsible for bending the trajectories of charged particles as they pass through the inner detector.
740 The three toroid magnets provide a field of 0.5 - 1 T and curve the path of muons passing through
741 the muon spectrometer.

742 The inner solenoid magnet is composed of over 9 km of niobium-titanium superconductor
743 wires, which are imbedded into strengthen pure aluminum strips. The solenoid is just 4.5 cm
744 thick, which minimizes interactions between the magnet material and particles passing through the
745 detector. It is housed in the LAr cryostat, as described in section 4.3.1, which further reduces the
746 amount of non-detector material required to support the solenoid. The return yoke of the magnet
747 is provided by the iron absorber of the TileCal [41].

748 The central ATLAS toroid magnet, providing the magnetic field for the barrel region of the MS,
749 is the largest toroidal magnet ever constructed at 25 m in length. The toroid is composed of eight
750 individual coils, each housed in their own cryostat. The toroidal magnetic field is advantageous
751 as the direction of the field is almost perpendicular to the path of the charged particles. 56 km of
752 aluminum stabilized niobium-titanium-copper superconductor wire compose the magnet. In each
753 end-cap, eight smaller superconducting coils extend the toroidal magnetic field to particles leaving
754 the detector in the forward direction [41]. Figure 4.9 shows the layout of the toroid magnets.

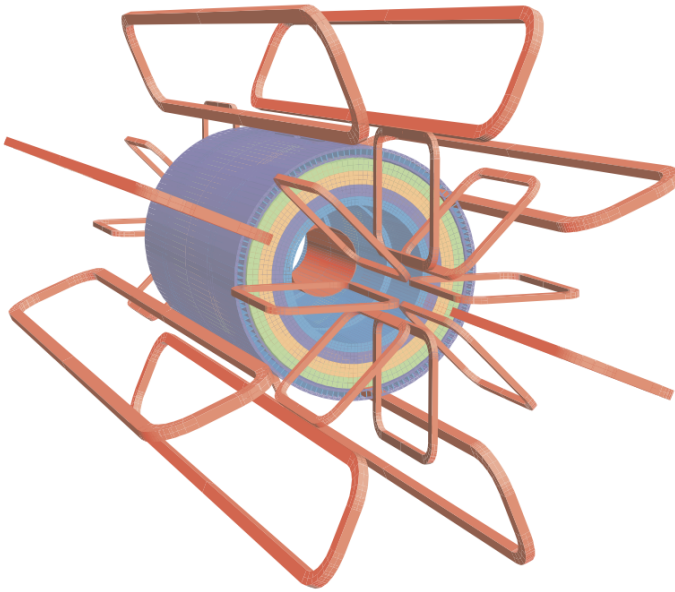


Figure 4.9: Layout of the barrel and endcap toroid magnets [32]

755 4.6 Forward Detectors

756 In addition to the inner detector, calorimeters, and muon spectrometer, three smaller detectors
757 provide coverage in the very forward region. The innermost forward detector, at 17 m from the
758 interaction point, is the **L**Uminosity measurement using **C**erenkov **I**ntegrating **D**etector (LUCID).
759 LUCID's primary purpose is to measure the relative online-luminosity for the ATLAS detector,
760 from inelastic $p - p$ scattering. The detector is composed of 20 aluminum Cerenkov tubes which
761 surround the beam pipe and face towards the interaction point.

762 The second forward detector is the Zero-Degree Calorimeter (ZDC), located 140 m from the
763 interaction point in both directions, at the point where the LHC beam-pipe divides into two separate
764 pipes. The ZDC's primary purpose is to detect forward neutrons from heavy ion collisions.

765 The third forward detector is the Absolute Luminosity For ATLAS (ALFA) system, located 240
766 m from the interaction point in both directions. ALFA determines luminosity by measuring elastic
767 scattering at small angles, from which luminosity can be calculated via the optical theorem. The
768 detector is built from scintillating fiber trackers. These are connected to the accelerator vacuum

769 via Roman pots, which allow the detector to come as close as 1mm to the beam without disrupting
770 the machine vacuum. The LUCID and ALFA detectors are crucial to determining the real-time
771 conditions of the beams and the total luminosity delivered to the ATLAS detector [32].

772 **4.7 Trigger and Data Acquisition**

773 The trigger and Data Acquisition systems (TDAQ) are responsible for selecting the most viable
774 events to save for further downstream processing. Because of the high luminosities delivered to
775 the ATLAS detector, not all events recorded can be saved; the 40 MHz bunch crossing rate must
776 be reduced by 5 orders of magnitude to an event storage rate of ~ 1 kHz. The trigger system is
777 composed of three distinct levels: Level 1 (L1), Level 2 (L2) and the event filter. Collectively the
778 L2 trigger and the event filter form the High Level Trigger (HLT).

779 The L1 trigger is implemented in the hardware of the ATLAS calorimeter and muon systems.
780 The primary modality of the L1 trigger is to identify muons, electrons, photons, jets, and τ -leptons
781 with high transverse momentum. Particles with high transverse momentum are more likely to
782 originate from direct, high energy collisions, which are most likely to produce interesting physics
783 processes. The L1 trigger also identifies events with large missing transverse energy, which could
784 be indicative of new physics. The L1 muon trigger (L1Muon) relies on RPC and TGC trigger
785 chambers in the barrel and end-cap regions of the muon spectrometer. The L1 Calorimeter Trigger
786 (L1Calo) uses reduced granularity information collected by all the calorimeter subsystems. Results
787 from the L1Muon and L1Calo triggers are combined by the Central Trigger Processor (CTP),
788 which implements a trigger ‘menu’, listing various combinations of trigger requirements. The
789 maximum L1 acceptance rate is 75 kHz, and the L1 trigger decision must reach the front-end
790 electronics within $2.5 \mu\text{s}$ of its associated bunch-crossing [32].

791 The L1 trigger defines a Region-of-Interest (RoI) for each passing event. The ROI is repre-
792 sented by the η - ϕ detector region where interesting features were identified by the L1 selection
793 process. Information about the type of feature identified and the threshold which was exceeded to
794 trigger the L1 response is also recorded. The ROI data is sent to the L2 trigger, which uses all of

795 the available information within the ROI at full granularity and precision. The L2 trigger reduces
796 the event rate from 75 kHz to 3.5 kHz, with an average processing time of 40 ms. The final stage of
797 the HLT is the event filter, which reduces the event rate to 200 Hz. The event filter uses an offline
798 analysis process to select fully rebuilt events which will be saved for further analysis.

799 All levels of the ATLAS trigger system depend on specialized electronics. Each detector front-
800 end system has a specialized Readout Driver (ROD) which collects information from several front-
801 end data streams at once. The ROD is composed of front-end analogue processing, an L1 buffer
802 which retains the information long enough for the L1 trigger decision, and dedicated links which
803 send the front-end L1 triggered data to Data Acquisition System (DAQ). Any digital signals are
804 formatted as raw data before being transferred to the DAQ. The first stage of the DAQ temporarily
805 stores the L1 data in local buffers. The ROI data is then requested by the L2 trigger, after which
806 selected events are transferred to an event building system, before events passing the event filter
807 are sent to the CERN computer center for permanent storage. The DAQ system not only allows
808 for the readout of detector data, but is also responsible for the monitoring and configuration of
809 the hardware and software components which make up the data readout system via the Detector
810 Control System (DCS).

811 The DCS allows centralized control of all detector subsystems simultaneously. It continually
812 monitors operational conditions, reports any abnormal behavior to the operator, and can perform
813 both automatic and manual interventions. The DCS reports on real time detector conditions such
814 as high or low voltage detector electronics, gas and cooling systems, magnetic field conditions,
815 humidity and temperature. This information is continually monitored by experts in the ATLAS
816 control room, so that action can be taken immediately to correct any issues that arise. The DCS also
817 handles communication between detector systems, and other systems such as the LHC accelerator,
818 the ATLAS magnets, and CERN technical services [32].

Chapter 5: Particle Reconstruction and Identification

821 With a design luminosity of $1.0 \times 10^{34} \text{ cm}^{-2}\text{s}^{-1}$, and a peak Run-2 instantaneous luminosity of
 822 $2.0 \times 10^{34} \text{ cm}^{-2}\text{s}^{-1}$, reconstructing and identifying the products of LHC $p p$ collisions is one of the
 823 most complex tasks for each LHC experiment. The accurate reconstruction and identification of
 824 physics objects lays the ground work for all subsequent physics analyses, so it is also one of the
 825 most fundamentally important tasks performed by an experiment.

826 Reconstruction is the process of combining raw and uncalibrated hits across various subsystems
 827 into specific unique objects. Two particular subsystems, the Inner Detector (ID) tracker and the
 828 calorimeters play particularly important roles and will be discussed in detail. Analysis of the
 829 properties of the reconstructed objects identifies them as photon, electrons, muons, or jets. While
 830 photons, electrons, and muons are fundamental particles, jets represent a collimated shower of
 831 many hadronic particles, whose definition is more flexible. Jet reconstruction, clustering and track
 832 association are all of particular import to jet identification, and to the later content of this thesis.
 833 Finally, reconstruction also identifies missing transverse energy E_T^{miss} in events, which is a crucial
 834 variable for BSM physics searches. Figure 5.1 shows how the physics objects listed here interact
 835 with various systems in the ATLAS detector.

836 5.1 Inner Detector Tracks

837 As the inner most layer of the detector, the ID measures charged particles close to the interac-
 838 tion point. The various hits of these charged particles throughout the ID are used to reconstruct
 839 *tracks* which give the trajectories of charged particles [43]. Track reconstruction begins by clus-
 840 tering hits in the Pixel and SCT detectors, and combining clusters from different radial layers of
 841 these detectors. The multi-layer clusters form track *seeds*, which provide initial estimates of mea-

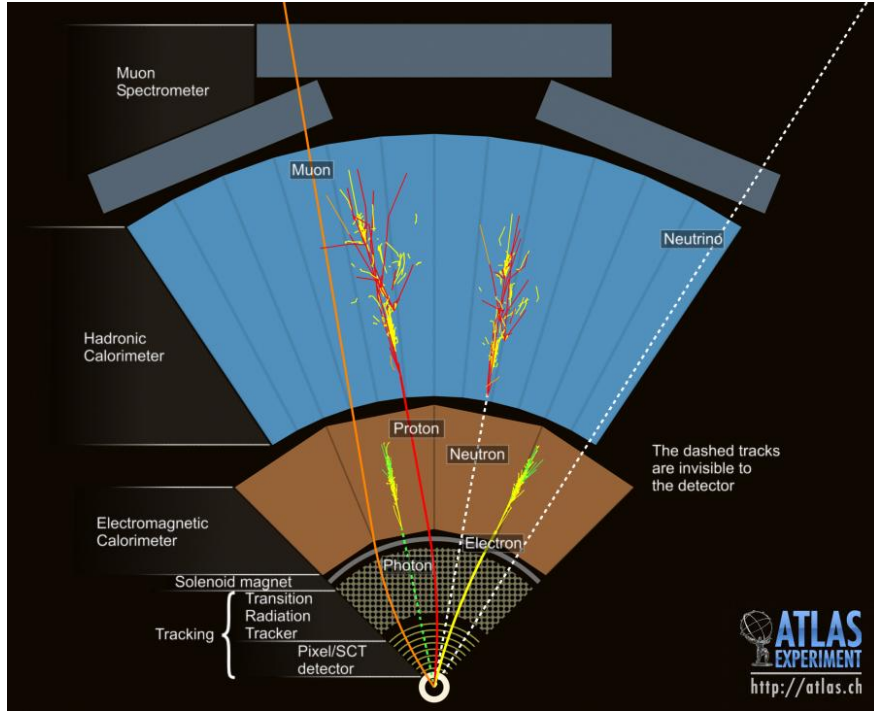


Figure 5.1: Graphic illustrating the various objects and high level features identified by ATLAS object reconstruction, and their interaction with different systems of the ATLAS detector [42]

842 measurements belonging to an individual track. The requirement of three points allows for a rough
 843 estimate of the track p_T to be made by calculating the curvature of the track and accounting of the
 844 magnetic field in the ID.

845 Track seeds are subject to a variety of quality requirements, such as having a minimum esti-
 846 mated p_T and passing interaction region compatibility criterion. If these requirements are satisfied,
 847 the track seeds are passed to the track finding and fitting algorithms. The interplay of these three
 848 track reconstruction steps is illustrated in Figure 5.2.

849 5.2 Photons and Electrons

850 Photons and electrons shower in the LAr calorimeter, and are identified by the energy deposits
 851 they leave there. Energy deposits in a collection of nearby cells are termed *clusters*, which become
 852 the starting point for electron and photon reconstruction [44]. The clustering algorithm begins
 853 when the energy deposit in a certain cell exceeds the noise threshold with a significance of 4σ .

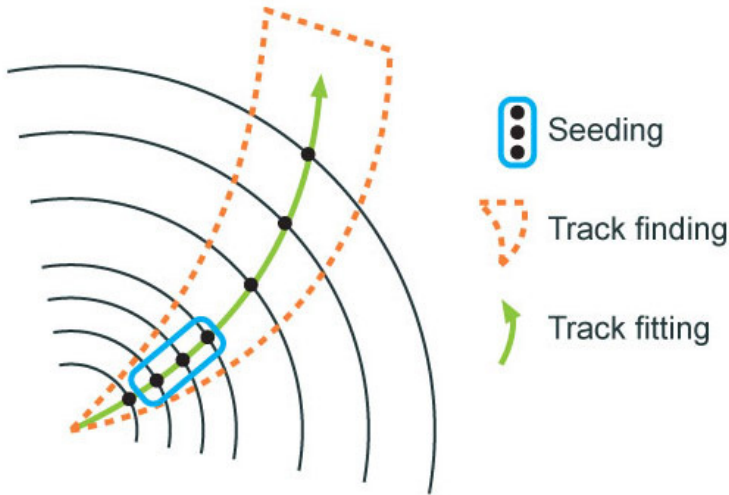


Figure 5.2: Track reconstruction seeding, finding and fitting illustration [43]

854 The algorithm then collects neighboring cells which have an energy deposit exceeding the noise
 855 threshold with a significance of 2σ , creating a topo-cluster. Next, these topo-clusters are matched
 856 to ID tracks, created as described in Section 5.1. The location of the topo-cluster defines a region
 857 of interest (ROI) in the ID, where additional modified track reconstruction algorithms are run in the
 858 case that no associated tracks are found. Any ID tracks associated to the topo-cluster are retrofitted to
 859 allow for additional energy loss due to bremsstrahlung. A converted photon track reconstruction
 860 algorithm is run to check for tracks coming from secondary vertices consistent with converted
 861 photons. The secondary vertices are constructed from two oppositely charged tracks consistent
 862 with a massless particle, or from one track without any hits in the innermost layer of the ID.

863 For electron identification, the EM cluster is required to match ID tracks that originate from
 864 the primary vertex at the interaction point. For photon identification, the EM cluster can either be
 865 matched to tracks coming from a secondary vertex (converted photon), or matched to no tracks
 866 (unconverted photon). Figure 5.3 illustrates these three cases for EM object identification.

867 *Superclusters* are built separately for photons and electrons, based on the combined topo-cluster
 868 and ID track information. First, the EM topo-clusters are tested to see if they meet the minimum
 869 requirements to become electron or photon seed clusters. For electrons, the cluster must have a
 870 minimum E_T of 1 GeV, and must be matched to a track with at least 4 hits in the silicon tracking

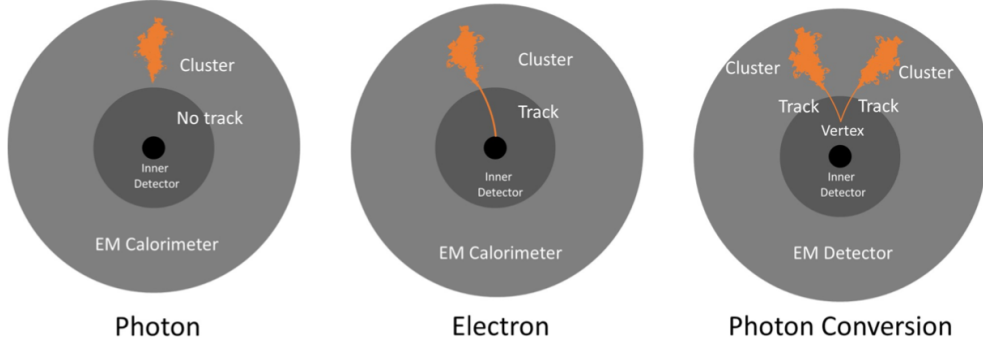


Figure 5.3: Three types of EM object candidates [45].

detectors. For photons, the cluster must have an E_T greater than 1.5 GeV. If the seed cluster requirements are met, the algorithm searches for satellite clusters, which can arise from bremsstrahlung radiation. If the satellite clusters pass the positional, energy and tracking requirements to be associated with the proto-cluster, they are combined into a supercluster.

Electron and photon objects are identified from the superclusters after energy calibration and position corrections are applied. Because photon and electron superclusters are built independently, some clusters can produce both a photon and an electron. In this case an ambiguity resolution procedure is applied to determine if the supercluster can be easily identified as only a photon (no tracks present) or only an electron (good tracks pointing to the primary vertex). In some cases, the identity of the cluster is still ambiguous, in which case both a photon and electron object are created for analysis and flagged as ambiguous. Energy, shower shape, and other analysis variables are calculated from the supercluster and saved with the electron or photon object.

5.3 Muons

Muons are identified through the tracks and energy deposits they leave in the ID, calorimeters, and Muon Spectrometer (MS). Muon identification begins in the Muon Drift Tube chambers by performing a straight line fit between the hits found in each layer, creating *segments*. Segments in the middle layers are then used as seeds for the track building algorithm, which searches for compatible combinations of segments based on their relative positions and angles [46]. A χ^2 fit is

889 performed on each track candidate. Based on the χ^2 criteria, hits are removed or added such that
890 the track contains as many hits as possible while satisfying the fit criteria.

891 The MS track candidates are combined with track information from the ID and calorimeters
892 according to various algorithms based on the information available from each subdetector. Four
893 different types of muons arise from the various reconstruction algorithms:

- 894 • Combined muon: a muon track identified through independent track reconstruction in the
895 ID and MS, where the combined track is formed using a global refit that uses hit information
896 from both detectors. Most muons are constructed through an outside-in procedure, in which
897 a muon track candidate is identified in the MS and then an associated track is found in the ID.
898 A complementary inside-out procedure is also implemented and identifies additional muons.
- 899 • Segment-tagged muon: an ID track is identified as a muon if when extrapolated out to the
900 MS (following the inside-out global fit procedure) it is matched to at least one local MS
901 segment.
- 902 • Calorimeter-tagged muon: an ID track is identified as a muon if it is matched to a calorimeter
903 energy deposit that is compatible with a minimum-ionizing particle. This muon identifica-
904 tion has the lowest purity, but it used in regions where the MS has only partial coverage due
905 to cabling and service access routes.
- 906 • Extrapolated muons: the muon is reconstruction only from the MS track and a requirement
907 on compatibility with the primary interaction point. The muon track is required to cross at
908 least two layers of the MS, and three layers in the forward region. These muons are mainly
909 used to extend muon acceptance into the region $2.5 < |\eta| < 2.7$ where ID track information
910 is not available.

911 Figure 5.4 illustrates the four types of muon reconstruction. Overlap between reconstructed
912 muons using ID tracks is resolved by giving preference to combined muons, then segment tagged
913 muons, and finally calorimeter tagged muons. Overlap with extrapolated muons is resolved by
914 giving preference to the muon with a better fit quality and higher number of tracks.

915 All muon track candidates are required to pass a series of quality selections to be identified in
 916 the final muon collection. The primary qualities considered are the χ^2 goodness of fit for the global
 917 track, the difference in p_T measurement between the ID and MS tracks, and the ratio between the
 918 charge and momentum of the tracks. The quality requirements help reject hadrons, primarily from
 919 kaon and pion decays. Muons candidates consistent with cosmic rays are also rejected.

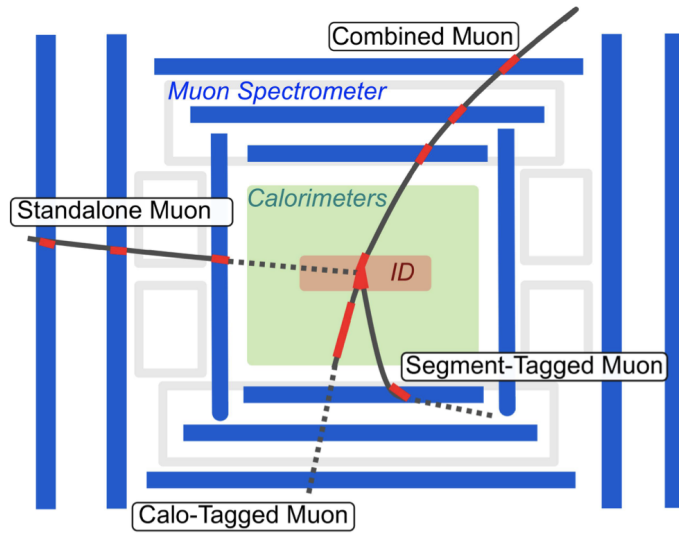


Figure 5.4: Four types of muon track candidates [47].

920 5.4 Jets

921 The protons accelerated in the LHC are composed of quarks and gluons, and thus their colli-
 922 sions often result in the release of energetic quarks and gluons, collectively termed *partons*. The
 923 energetic partons can radiate additional gluons, and these gluons can pair produce quarks in a pro-
 924 cess called *fragmentation*. Fragmentation continues until the energy drops sufficiently that color
 925 conservation plays a dominant role. At that point, additional quarks and gluons are produced from
 926 vacuum to create neutral color states for the fragmented collection of partons. This process is
 927 known as *hadronization* [48]. The hadronized partons compose a collimated stream of particles,
 928 known as a *jet*, which is then observed in the detector. The full process that produces jets is known
 929 as a *parton shower*, and is illustrated in Figure 5.5.

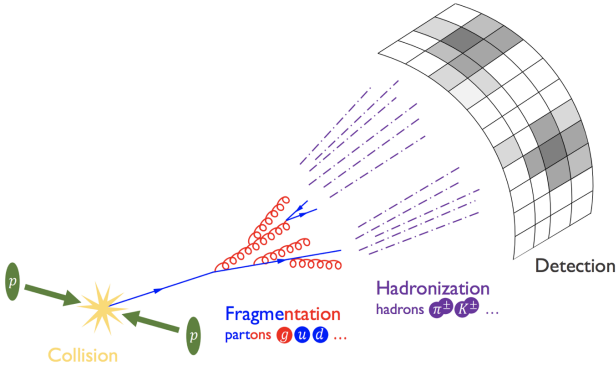


Figure 5.5: The fragmentation and hadronization processes undergone by a quark produced in a proton-proton collision [49].

930 Jets are identified by the energy deposits they leave in the calorimeter, which are then matched
 931 to the tracks they leave in the ID. Jet reconstruction generally begins in the calorimeters, with the
 932 identification of *topo-clusters*. Then jet reconstruction algorithms combine calorimeter informa-
 933 tion with tracking information. The anti- k_t algorithm [50] as provided by the FastJet library [51] is
 934 generally used by the ATLAS experiment, with varying reconstruction radius settings. There are a
 935 variety of jet collections depending on the exact usage of calorimeter and tracking information in
 936 the reconstruction. Some common collections include particle flow jets (PFlow), track calo-cluster
 937 jets (TCC), EM topo-cluster jets (EMTopo), and unified flow object jets (UFO). Only particle flow
 938 jets will be discussed in greater detail due to their importance in this analysis. The following sec-
 939 tions discuss jet identification in the calorimeters, particle flow jet construction using the anti- k_t
 940 algorithm, jet clustering and jet substructure characteristics.

941 5.4.1 Calorimeter Clusters

942 Jets are first identified by the energy deposits they leave in the calorimeters. The reconstruc-
 943 tion of jets in ATLAS begins with the construction of *topo-clusters*, which are topologically-grouped
 944 noise-suppressed clusters of calorimeter cells [52]. The topo-cluster seed is a cell with an energy
 945 that is at least 4× the average background noise level for the cell. Any cells adjacent to the seed
 946 cell in three dimensions are added to the cluster if they have an energy deposit that is at least 2x

947 the average expected noise. This process is repeated, growing the cluster, until no adjacent cells
948 exceeding the energy deposit threshold remain. As a final step, all adjacent cells are added to the
949 topo-cluster, irrespective of their energy.

950 The construction process for topo-clusters allows for the possibility that several independent
951 signatures are grouped into one topo-cluster. To correct for this, the topo-cluster is scanned for
952 local maximum, defined by any cell with energy > 500 MeV, and no neighboring cells with greater
953 energy. If more than one local maximum is identified, the topo-cluster is split among the corre-
954 sponding energy peaks [53]. In the event that one cell neighbors two or more local maxima, the
955 cell is assigned to the two highest-energy clusters that is neighbors. This means each cell is shared
956 at most once, between at most two post-splitting topo-clusters.

957 Two measurements for the total energy of the topo-cluster are considered. The raw, or electro-
958 magnetic (EM), scale simply considers the sum of energy from all cells in the topo-cluster. The
959 local cell weighting (LCW) scale first classifies clusters as electromagnetic or hadronic, and then
960 applies appropriate corrections for hadronic interactions in the jet energy calculation [52]. The
961 corrections are derived from Monte Carlo simulations, and account for the weaker response of
962 ATLAS calorimeters to hadronic interactions (ATLAS calorimeters are *non-compensating*), and
963 hadronic energy losses due to interactions with dead material [53].

964 5.4.2 Particle Flow Algorithm

965 The calorimeters provide excellent jet energy resolution for high energy jets. However, the
966 granularity of the hadronic calorimeter is restricted to 0.1×0.1 in $\eta \times \phi$. Combining the infor-
967 mation from the calorimeter with tracking information provides superior angular resolution and
968 energy resolution. The particle flow (PFlow) algorithm is one of a handful of algorithms which
969 can perform this task.

970 An overview of the process is given in Figure 5.6. Tracks from the ID which are selected for the
971 PFlow algorithm are required to have at least 9 hits in the silicon detector, and missing pixel hits in
972 places where a hit would be expected. Additionally, the tracks have $p_T > 0.5$ GeV, and $|\eta| < 2.5$.

973 The algorithm then attempts to match these tracks to EM scale calorimeter topo-clusters. This
974 matching is performed using the distance metric

$$\Delta R' = \sqrt{\left(\frac{\Delta\phi}{\sigma_\phi}\right)^2 + \left(\frac{\Delta\eta}{\sigma_\eta}\right)^2} \quad (5.1)$$

975 where σ_η and σ_ϕ represent the angular widths of the topo-clusters, and $\Delta\eta$ and $\Delta\phi$ represent the
976 distance between the track, extrapolated to the second layer of the EM calorimeter, and barycenter
977 of the topo-cluster [54]. The topo-cluster closest to the track as measured by $\Delta R'$ is considered
978 matched to the track. If no topo-cluster is found within the cone size of $\Delta R' = 1.64$, it is assumed
979 that particle which left the track did not form a topo-cluster in the calorimeter.

980 The PFlow algorithm predicts the expected single topo-cluster energy for a given track, based
981 on the track momentum and topo-cluster position. This value is then compared to the observed
982 energy of the topo-cluster, and the probability that the particle energy was deposited in more than
983 one topo-cluster is evaluated. If necessary, the algorithm adds more topo-clusters to the track/topo-
984 cluster system, in order to account of the full shower energy of the track particle.

985 To reduce the impact of double counting the energy of a given particle by including both its
986 tracker and calorimeter energy measurements, the calorimeter energy measurements associated to a
987 given track are subtracted from the total calorimeter measurement. If the expected energy deposited
988 by the particle exceeds the topo-cluster energy, the full topo-cluster is removed. If the expected
989 energy is less than the EM scale energy of all the considered topo-clusters, topo-cluster cells are
990 removed one by one, until the full expected energy deposit of the particle has been removed from
991 the calorimeter information. The resulting set of tracks and topo-clusters represent the event with
992 no double-counting of energy between subdetectors [54]. This information is passed to the jet-
993 finding algorithm.

994 5.4.3 Jet Clustering

995 When a parton decays in the detector, its energy deposits often result in multiple calorimeter
996 clusters. For physics purposes, it is useful to combine clusters that likely resulted from an individ-

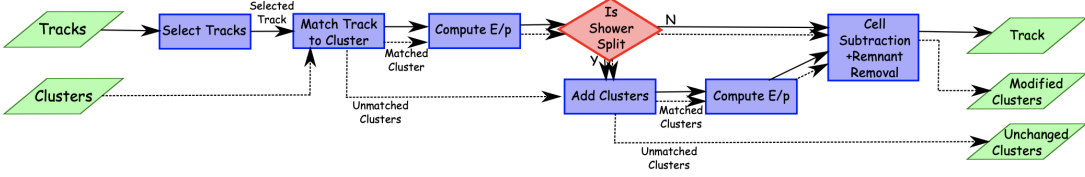


Figure 5.6: A flow chart illustrating the particle flow algorithm progression [54].

997 ual parton decay, in order to reconstruct the parton. The process of grouping topo-clusters which
998 were produced by the same parton decay is *jet clustering*.

999 The anti- k_t algorithm is the most commonly used algorithm for jet clustering in ATLAS. The
1000 anti- k_t algorithm is based on sequential recombination algorithms [55]. A sequential recombina-
1001 tion considers the distance d_{ij} between objects i and j (particles or pseudojets), and the distance
1002 d_{iB} between an object i and the beam line B . If d_{ij} between two objects is the smallest distance
1003 among those considered, i and j are combined into a pseudojet. The process continues until the
1004 smallest distance is d_{iB} at which point the object i is determined to be a jet and removed from the
1005 objects in consideration. The procedure is repeated with the remaining objects until there are none
1006 remaining [50].

1007 The anti- k_t algorithm adopts this procedure, but modifies the distance measurements d_{ij} and
1008 d_{iB} to consider the transverse momentum k_t :

$$d_{ij} = \min(k_{ti}^{2p}, k_{tj}^{2p}) \frac{\Delta_{ij}^2}{R^2}, \quad (5.2a)$$

$$d_{iB} = k_{ti}^{2p}. \quad (5.2b)$$

1009 The addition of the term p allows adjustments to algorithm which govern the relative power of
1010 the momentum versus the geometrical scale $\Delta_{i,j}$, which is defined as $\Delta_{i,j} = (y_i - y_j)^2 + (\phi_i - \phi_j)^2$
1011 where y_i and ϕ_i are respectively the rapidity and azimuth of particle i [50]. The radius parameter
1012 R is chosen and determines the geometric cone size [55].

1013 In the case $p = 1$ the inclusive k_t algorithm [55] is recovered, which is a standard sequential

combination jet clustering algorithm. In the case $p = 0$, the Cambridge/Aachen sequential combination algorithm [56] is recovered. The case $p = -1$ gives rise to the anti- k_t algorithm. The impact of this choice means that the distance d_{ij} between many soft particles is larger than between soft and hard particles. Therefore, soft particles tend to cluster with hard ones before they cluster with other soft particles. They key feature of this behavior is that soft particles do not modify the shape of the jets. This leads to the creation of circular conical jets, a desirable feature which sequential combination algorithms and cone algorithms struggle to achieve. Figure 5.7 compares anti- k_t jet formation with the inclusive k_t and Cambridge/Aachen algorithms mentioned here, as well as the SIScone algorithm [57], which checks for sets of stable cones compatible with the observed radiation.

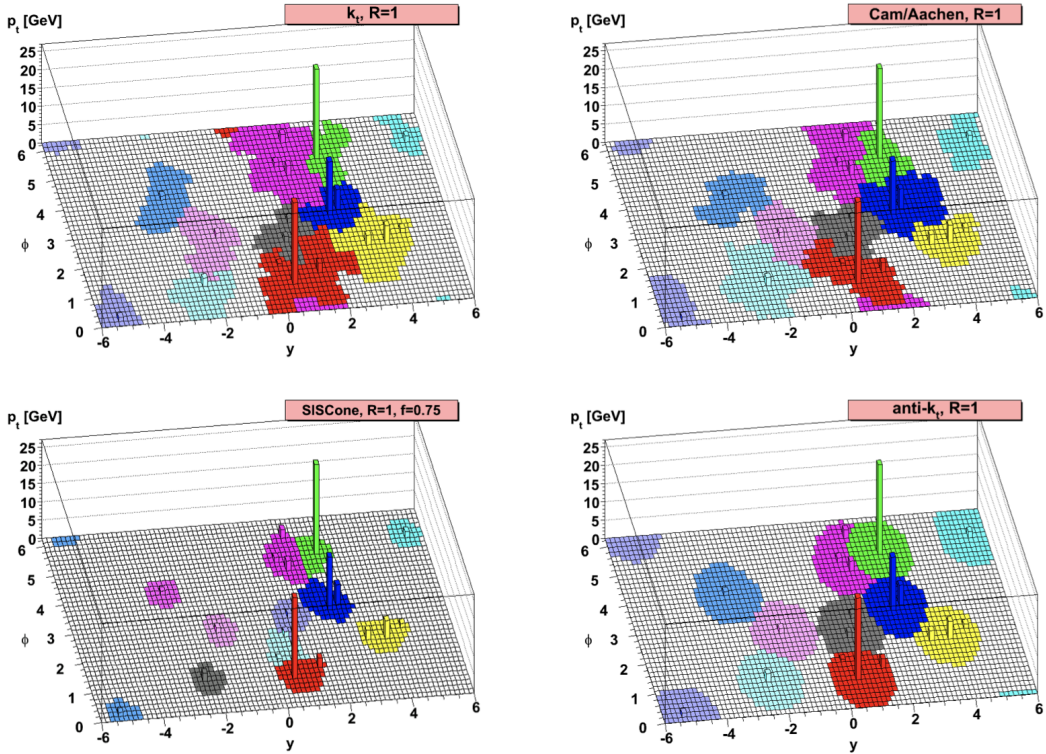


Figure 5.7: A comparison of jet clustering with four different jet algorithms. The anti- k_t algorithm is observed to create the most conical jets, where the shape of the jet is immune to the presence of soft radiation [50].

Any useful jet clustering algorithm must satisfy the requirements of infrared safety and collinear

1025 (IRC) safety. Infrared safety implies that the resulting set of jets is unaltered by the presence of
1026 additional soft particles in the list of seed clusters. As explained above, the anti- k_t algorithm is
1027 natural infrared safe. Collinear safety requires that the final set of jets is not impacted by collinear
1028 splitting of one of the jets. If the hardest particle p_1 is split into a collinear pair (p_{1a}, p_{1b}) (as
1029 is common in the fragmentation process for a hard parton), the jet clustering algorithm must
1030 still recognize (p_{1a}, p_{1b}) as the hardest jet in the collision. If another softer particle p_2 with
1031 $p_{t,1a}, p_{t,1b} < p_{t,2} < p_{t,1}$ is instead considered the hardest particle in the event, a different final
1032 set of jets would be returned. Collinear safety is a requirement of perturbative QCD, to ensure
1033 non-divergent higher-order calculations [58]. The anti- k_t algorithm's tendency to cluster hard par-
1034 ticles first ensures its collinear safety. By satisfying the IRC safety requirement, anti- k_t jets can be
1035 calculated using perturbative QCD, which improves comparisons with theory.

1036 5.4.4 Ghost Track Association

1037 Once a collection of jets has been created, the jet objects can be studied at both the event-level
1038 and the jet-level. In the event-level picture, the momentum, energy, and geometric orientation
1039 of the jets within an event are considered. This yields important information about decay of any
1040 resonant heavy objects, the total energy in the event, and the distribution of energy amongst the jets.
1041 At the jet-level picture, the particles composing the jet are considered. The momentum, energy,
1042 and geometric orientation of the particle tracks provides a low-level picture of the jet, which can
1043 help determine if the properties of the jet are consistent with standard QCD, or if new physics
1044 processes might be represented within the patterns found in the constituent particles. Jet-level
1045 analysis is also widely used in flavor tagging.

1046 For anti- k_t jets with a radius parameter $R = 0.4$, one way of studying the jet-level picture
1047 is through considering the ghost-associated tracks. Track association is process of determining
1048 which tracks should be considered associated with a given jet. In the ghost association algorithm,
1049 the anti- k_t clustering algorithm is used for the collection of tracks and calorimeter clusters [59].
1050 However, the tracks are considered to have infinitesimal momentum (*ghosts*), so their addition to

1051 a jet object does not alter the four-momentum of the jet. This ensures the final jet collection is not
1052 altered by the presence of the ghost tracks in the reclustering, but information about the associated
1053 tracks for each reconstructed jet becomes available [60].

1054 Ghost tracks are of particular importance to this analysis, as a means of providing a low-level
1055 picture of the shape of $R = 0.4$ jets, and discriminating Standard Model QCD-like jets from dark
1056 QCD-like jets.

1057 **5.5 Missing Transverse Energy**

1058 A simple principle leveraged in ATLAS physics analyses is checking for conservation of mo-
1059 mentum among the products of any pp collisions. The initial state transverse momentum of any
1060 pp collision is always zero, so the transverse momentum of all final state particles should likewise
1061 be zero. The missing transverse energy, E_T^{miss} , is determined by the magnitude of the negative
1062 momentum vector sum of all final state objects resulting from the pp collision.

1063 Specifically, the objects considered in the E_T^{miss} calculation are photons, electrons, muons, jets,
1064 and soft terms. The first four items comprise the hard components of the E_T^{miss} calculation, and
1065 have been discussed previously in this chapter. The final item represents a collection of *soft terms*,
1066 comprising any detector signals not associated to hard detector objects. These can be based on
1067 unassociated tracks, or unassociated soft calorimeter clusters. Both are generally not used in the
1068 same calculation to avoid double counting of soft terms. In this analysis the calorimeter cluster
1069 soft terms are considered in the E_T^{miss} calculation.

1070 E_T^{miss} can arise due to non-interacting Standard Model objects such as neutrinos, fake sources
1071 such as mis-reconstructed objects and dead detector regions, or in some theories, non-interacting
1072 BSM objects such as a dark matter candidate particles. To understand the amount of E_T^{miss} at-
1073 tributable to detector noise and mis-reconstruction, E_T^{miss} is studied in $Z \rightarrow \mu\mu$ where little real
1074 E_T^{miss} is expected [61]. As Figure 5.8 illustrates, the resolution of E_T^{miss} generally decreases as
1075 E_T^{miss} increases, due to detector resolution effects. As E_T^{miss} is an important quantity for most dark
1076 QCD analyses, limitations in the accuracy of the E_T^{miss} calculation must be considered.

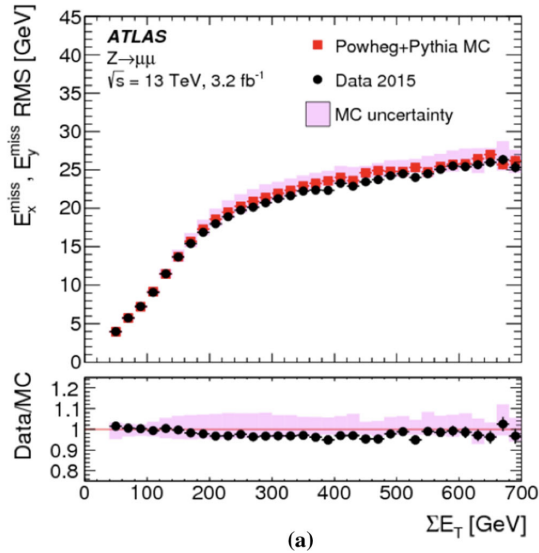


Figure 5.8: A comparison of MC simulation and data for $Z \rightarrow \mu\mu$ events where real $E_T^{\text{miss}} = 0$ [61]. The resolution of the missing energy in the transverse ($x - y$) plane is observed to increase with increasing total $\sum E_T$.

1077

Part III

1078

Search

1079

1080

Chapter 6: Machine Learning Tools

1081 This analysis relies on machine learning tools that train over low-level information, namely
1082 tracks of the leading two jets. The subtlety of the shower differences between dark and SM QCD
1083 motivates a complex model that can accept high-dimensional low-level inputs to best understand
1084 key differences between signal and background correlations. Events used in the training of ML
1085 tools and to which ML-based selections are applied are subject to the analysis level preselection
1086 described in Section ???. All models and training code can be found in Gitlab¹.

1087 6.0.1 Particle Flow Network (Supervised)

1088 The supervised analysis approach is one where the ML method is built to maximize exclusion
1089 sensitivity to the generated SVJ signal models. Here, supervised refers to the use of full and correct
1090 labels for all events considered during model training. We choose our architecture for two reasons:
1091 *permutation invariant input modeling* to best describe the events consisting of an unordered set
1092 of particles, and a *low-level input modeling* (over tracks) to take advantage of the available high-
1093 dimensional information to best exploit available correlations within the event.

1094 A Particle Flow Network (PFN) [**pfm**] is used to model input events as an unordered set of
1095 tracks. Given the inherently unordered and variable-length nature of particles in an event, this
1096 choice of modeling as a *set* can enable the model to better learn the salient features of the dataset
1097 that enable a signal-to-background classification. Constructing the PFN involves the creation of
1098 new basis variables \oplus for each particle in the event. Permutation invariance is enforced by summing
1099 over the per-particle unordered representation to create a new permutation invariant latent space
1100 basis O . Finally the classifier F is a function of the sum over this new basis.

1101 Figure 6.1 gives a graphical representation of the use of summation in the PFN over per-particle

¹<https://gitlab.cern.ch/jgonski/svj-vae/>

info to create a permutation-invariant event representation.

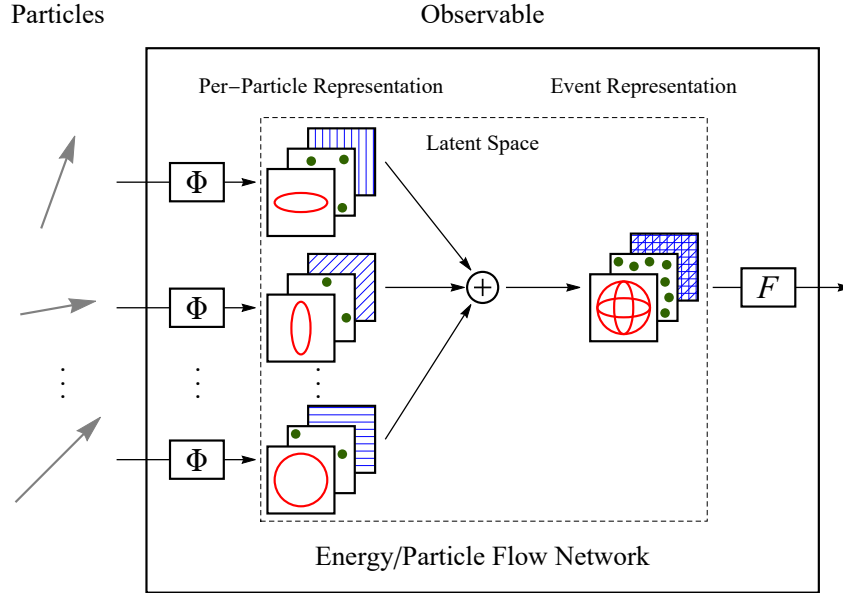


Figure 6.1: The Energy/Particle Flow Network concept, from Ref. [pfn].

1102

1103 In this implementation, we consider all tracks from the leading and subleading jets to create
 1104 an event level picture using track information that focuses on the objects that are likely to be
 1105 associated to the signal process. Figure 6.2 provides an annotated diagram of the PFN architecture
 1106 as used in this analysis.

1107 Input Modeling, Scaling, and Rotation

1108 Each track is described using seven variables: the four-vector of the track (p_T , η , ϕ , E), and
 1109 the track impact parameters d_0 and z_0 . Q/P was used in earlier versions of the PFN, but was
 1110 removed under further study as documented in Appendix ???. Up to 80 tracks per jet are allowed,
 1111 which is a threshold chosen to generally include all the tracks in the jet, which leads to maximal
 1112 performance. Figure 6.3 shows the track multiplicity in the leading and subleading jet for the signal
 1113 and background samples used in training.

1114 These tracks (up to 160 total) are given to the PFN as a single object. The two leading jets and
 1115 their associated tracks are rotated so that the center of the system is aligned with $(\eta, \phi) = (0, 0)$.

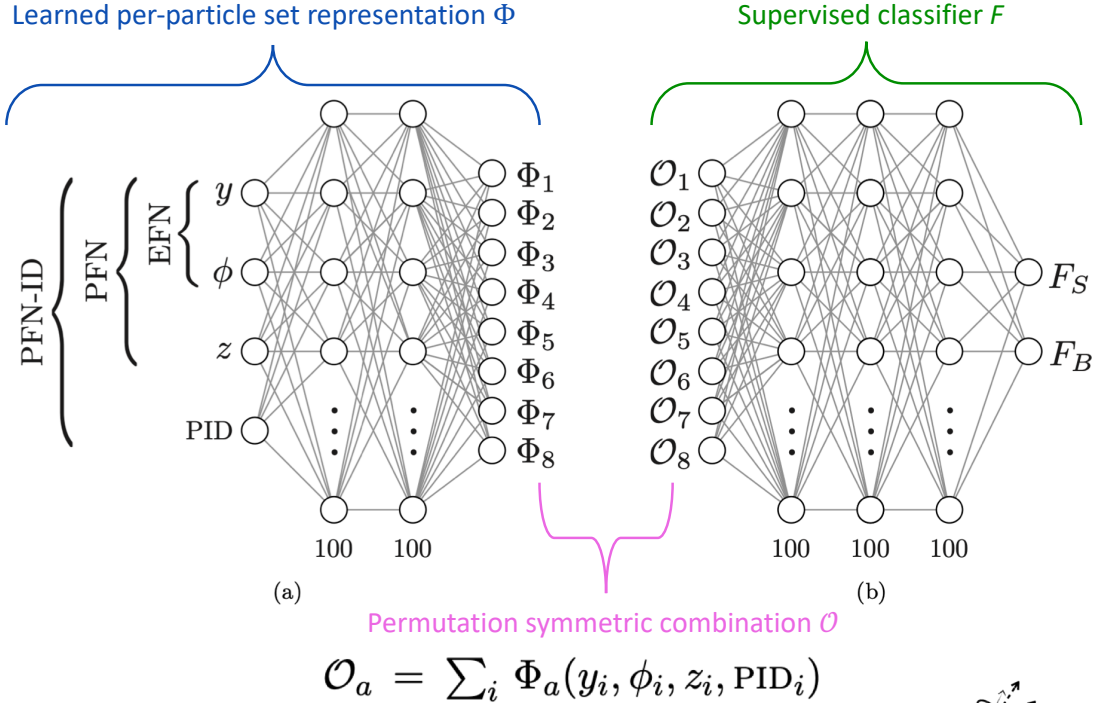


Figure 6.2: An annotated diagram of the PFN architecture.

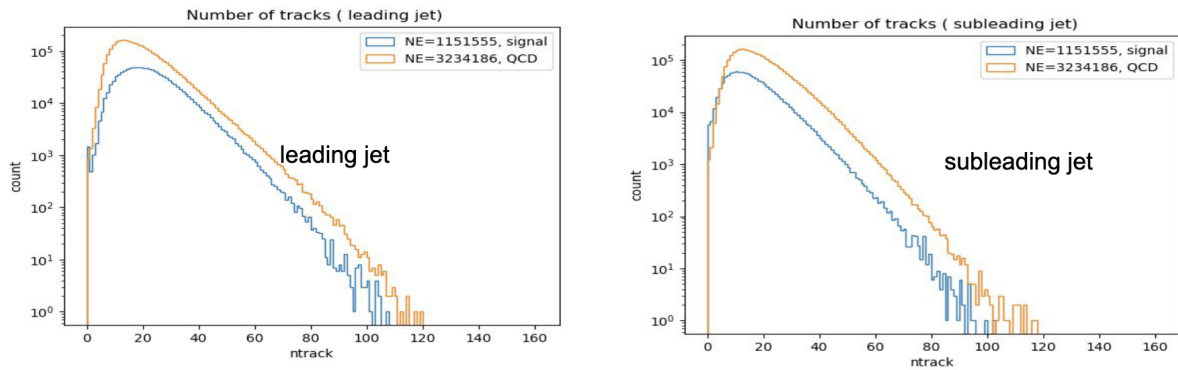


Figure 6.3: Distributions of the track multiplicity in the leading and subleading jets, comparing signal and background PFN training samples.

1116 Each track is normalized to its relative fraction of the total dijet system energy and transverse
 1117 momentum- this enforces agnosticism to the total energy and transverse momentum of the event.
 1118 Finally, each of the 6 track variables is scaled so that its range is [0,1]. Figure 6.4 illustrates the
 1119 rotation process.

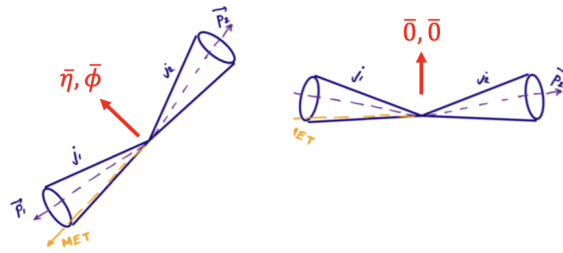


Figure 6.4: A diagram demonstrating how the two jet system is rotated in (ϕ, η) .

1120 Figure 6.5 and Figure 6.6 show each of 7 track variables. Figure 6.5 illustrates that the data
 1121 is well modeled by the MC at track level. Figure 6.6 shows the level of kinematic difference be-
 1122 tween the signal and background at track level, and demonstrates the impact of the rotation/scaling
 1123 procedure on the distributions.

1124 Training

1125 As seen in Figure 6.2, two separate architectures are defined and combined to do the supervised
 1126 training. The PFN uses a masking layer to suppress any zero-padded inputs, making the architec-
 1127 ture length agnostic. Additionally, a summation layer in the PFN enforces permutation invariance,
 1128 so the network is unordered. The Φ network has 3 dense layers of dimensionality 75 with RELU
 1129 activation, with 27.5k trainable parameters and an output Φ latent space dimension of 64. The
 1130 classifier F network similarly has 3 dense layers with 75 nodes with RELU activation, and a final
 1131 softmax layer to determine the event-level classification with a categorical cross-entropy loss. The
 1132 Adam optimizer is used with an initial learning rate of 0.001.

1133 The PFN is trained in a fully supervised way using SVJ signal MC and QCD MC events. Al-
 1134 though several SM processes are expected to contaminate the SR (see Section ??), QCD is the
 1135 dominant background. We found that training against a QCD-only sample produced better results

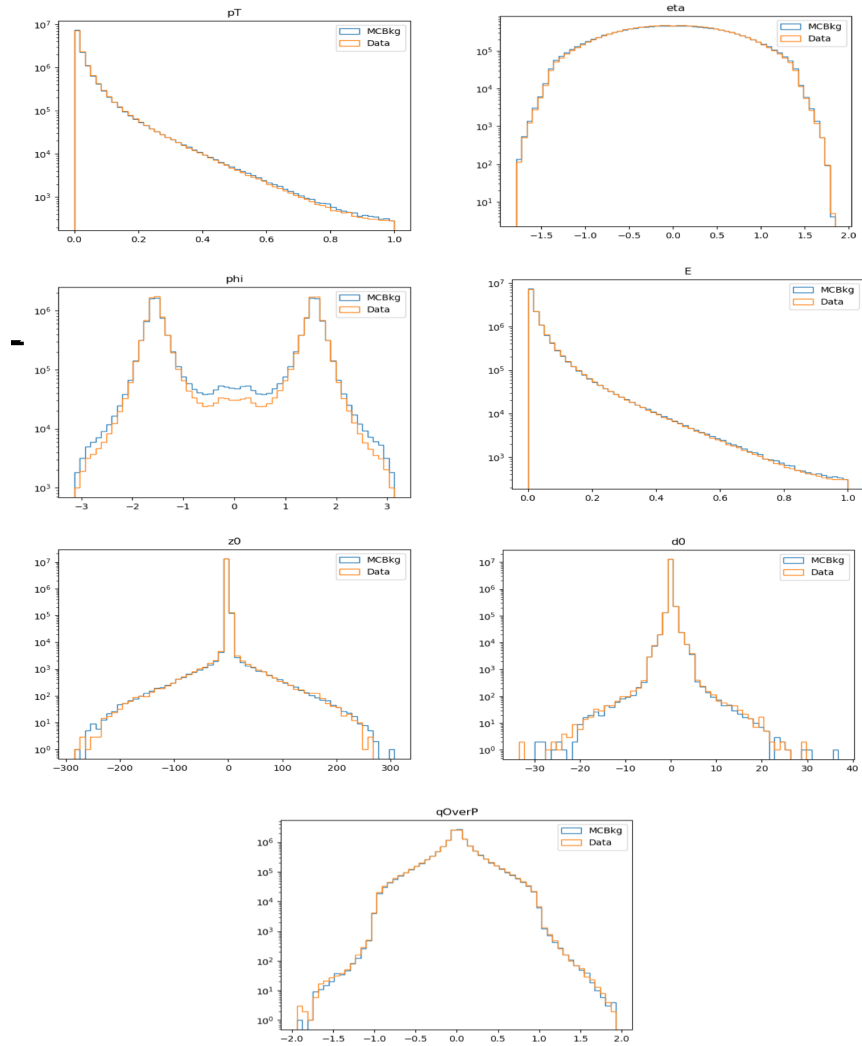
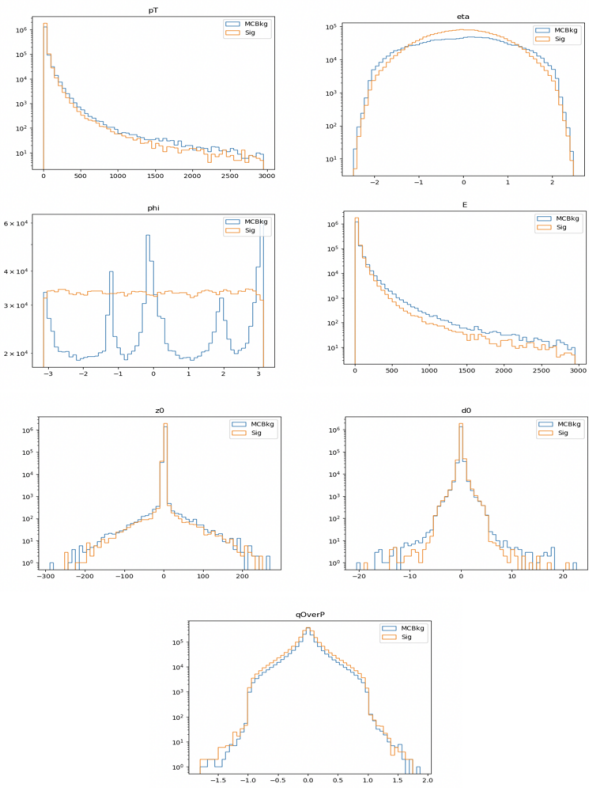


Figure 6.5: The 7 PFN track variables in data and background MC, after the scaling and rotation procedure is applied. We see excellent modeling of the data by the MC within the track variables.

Kinematic Inputs



Rotated & Scaled Inputs

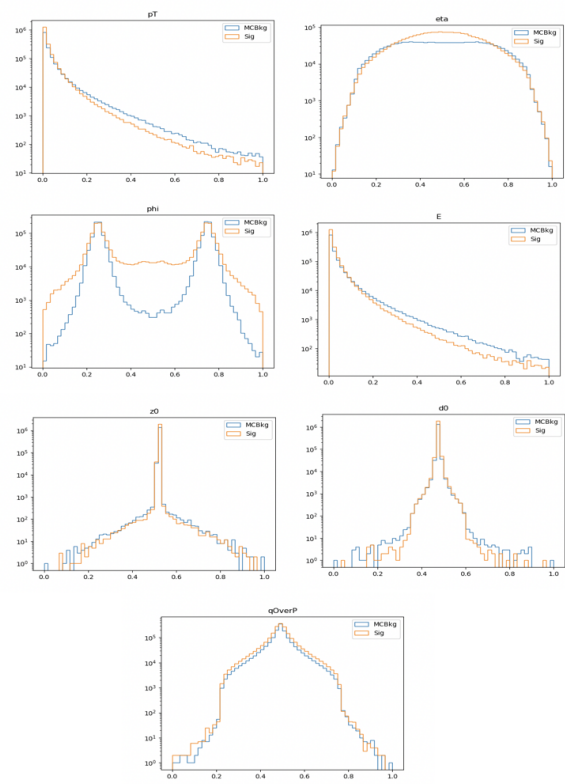


Figure 6.6: The 7 PFN track variables in background MC and signal MC. We see some differences between signal and background, but the track kinematics are largely similar.

1136 than training on a more complete background - when training with a background which repre-
 1137 sents samples that are more enriched in E_T^{miss} , the ability of the PFN to identify high E_T^{miss} signals
 1138 is reduced. When training with a QCD-only background, there is greater contamination from
 1139 E_T^{miss} enhanced backgrounds in the final SR - however the increased signal acceptance means that
 1140 overall sensitivity is still higher with a QCD-only training. This can be seen in the comparison of
 1141 output classifier distributions in Figure 6.7.

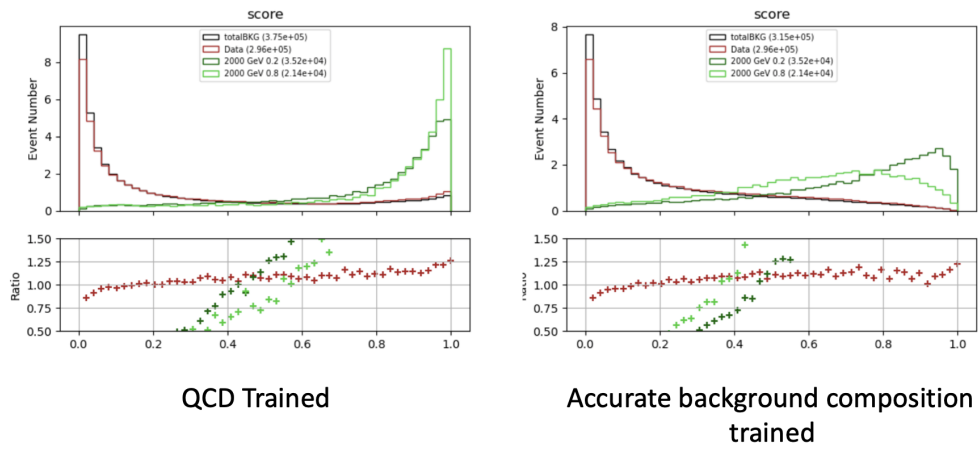


Figure 6.7: PFN score for background MC, data, and signal, comparing a PFN training on QCD-only vs all-background MC samples. The average AUC for the QCD-only training (left) is 0.93, while the average AUC for the mixed background training (right) is 0.84. The sensitivity estimate across the grid is better for the QCD-only training - from the distribution we can conclude that this is because the sensitivity to MET enhanced signals is greatly reduced.

1142 500k events from both background and signal are used in training, where the signal is a com-
 1143 bined file of all simulated signal points and the QCD background uses JZ slices 3-12 that are
 1144 sampled to produce the properly weighted p_T input shape. A train/test/validation split of 78%,
 1145 20%, and 2% is used for the final PFN training. In the tool development process, larger values
 1146 for test datasets were used to ensure good performance. A k-fold validation check is available in
 1147 Appendix ???. A study was done to check the optimality of the inclusive signal model PFN as
 1148 compared to one trained on high and low R_{inv} points separately, to better capture the differences
 1149 in high and low E_T^{miss} across signals and backgrounds, but a small effect is found and the decision
 1150 is taken to keep the inclusive model (Appendix ??). The network is trained for 100 epochs. Fig-
 1151 ure 6.14 shows the loss during training, which is stable and flattens by the end of training, and the

final evaluated losses that provide signal-background discrimination over the test set.

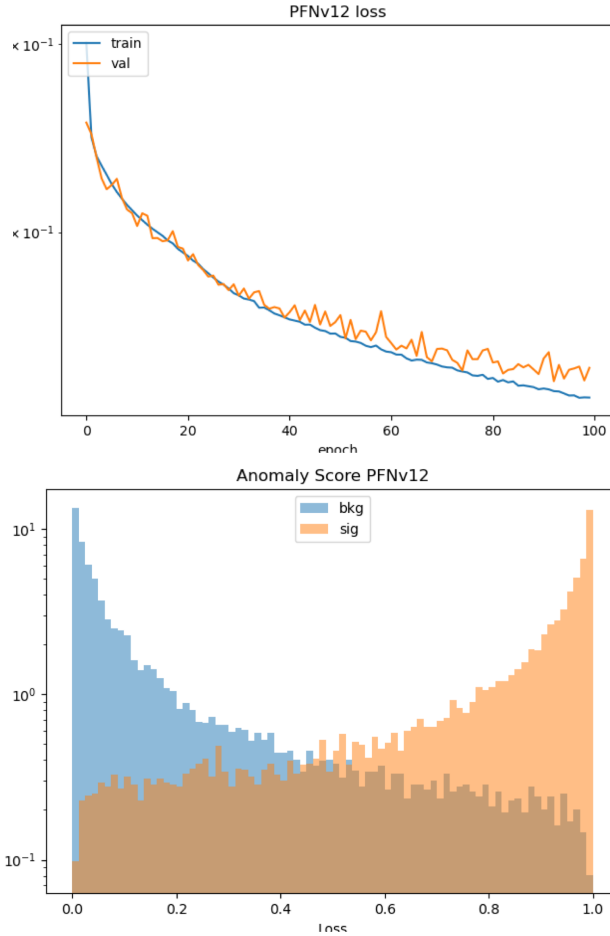


Figure 6.8: PFN architecture loss during training as a function of epoch (left) and the evaluated loss over the signal and background (right).

1152

1153 Optimization studies were performed on the PFN, varying the number of training epochs, num-

1154 ber of training events, batch size, learning rate, number of neurons, and dimension of the Φ space².

1155 The model presented here represents the optimal choice across these parameters.

1156 Performance

1157 The performance of the PFN can be assessed via the area-under-curve (AUC) of the receiver

1158 operating characteristic (ROC) associated to evaluating the PFN on the test set of signal and back-

1159 ground events. Figure 6.9 shows the ROC curve of the PFN when classifying the QCD background

²<https://indico.cern.ch/event/1294848/contributions/5441463/>

from the combined signal, with an AUC of 0.93. Figure 6.10 shows the AUC of the PFN across the SVJ signal grid, demonstrating strong discrimination capability even in the varying corners of phase space. Figure 6.11 shows the output score distribution in two signals, data, and the total background MC. A selection of PFN score > 0.6 for all SR events is chosen to maximize signal sensitivity across the grid.

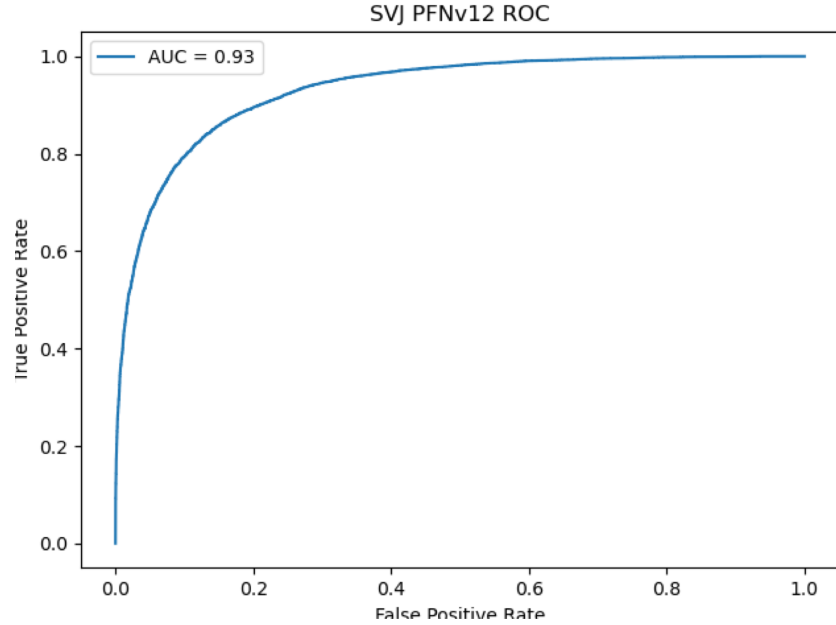


Figure 6.9: ROC the PFN score for combined signal (true positive) and QCD background (false positive).

Another supervised approach was studied using a BDT as the primary selection tool, trained over high-level variables describing each event. Studies comparing the PFN and BDT approaches are provided in Appendix ???. Ultimately the low-level high-dimensional approach offered by the PFN was selected for its increased performance and lessened kinematic dependence.

Appendix ?? shows more studies on the ML methods and comparisons of varying approaches.

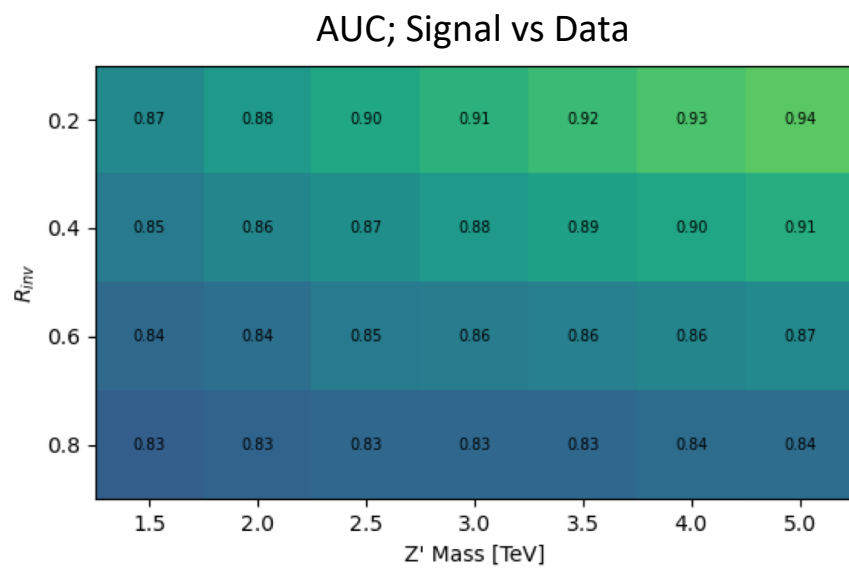


Figure 6.10: AUC from the PFN score for each signal in the SVJ grid, shown versus the QCD-only training sample.

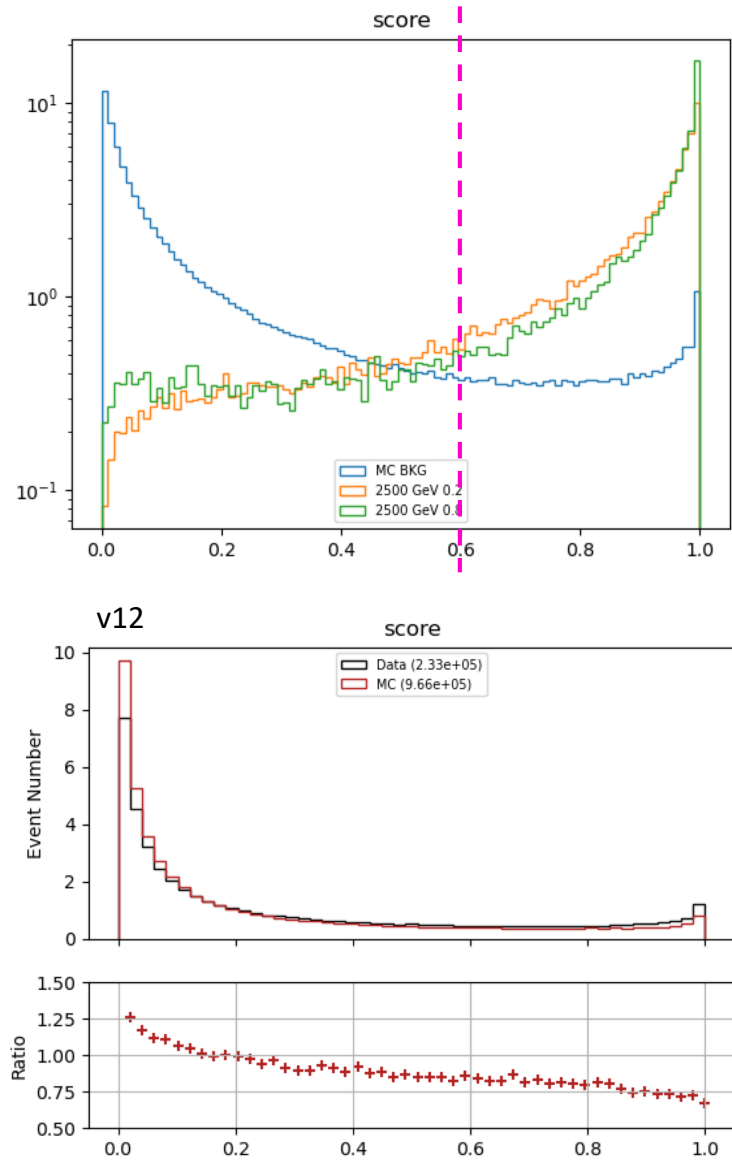


Figure 6.11: PFN score for two signals and the total background MC (top), and between data and MC (bottom). The difference between data and MC efficiency is minimal (< 5%).

1170 6.0.2 ANTELOPE (Semi-supervised)

1171 The semi-supervised analysis approach broadens the discovery sensitivity of the search through
1172 the use of semi-supervised ML, where training of the model is data-driven and labels are only
1173 partially provided during training. While broad sensitivity is a general key goal of LHC searches,
1174 it is particularly motivated in the case of dark QCD models, which can lead to widely varying
1175 topologies depending on the values of model parameters. In the case of SVJs, the R_{inv} fraction in
1176 the jet can dramatically vary the E_T^{miss} , shower shape, and other key features, making it difficult to
1177 find a single standard analysis variable that can distinguish all signal topologies from QCD.

1178 The model-independent search region of this analysis is implemented with a novel ML ap-
1179 proach that builds on the ANTELOPE architecture to construct a tool that is capable of performing
1180 low-level anomaly detection with permutation-invariant inputs. This tool, referred to as **ANomaly**
1181 **deTEction on particLe flOw latent sPacE (ANTELOPE)**, is a custom solution designed for this
1182 analysis.

1183 ANTELOPE uses the supervised signal vs. background training of the PFN network described
1184 in the previous section to generate a permutation invariant latent space that is representative of the
1185 original input variables, encodes the input events into these latent space variables O , and trains a
1186 *variational autoencoder* (VAE) over the events modeled as PFN latent space variables. The PFN
1187 latent space is a fixed length, unordered embedding of the original particles given as input to the
1188 model. A visual example of the ANTELOPE inputs is given in Figure 6.12.

1189 The VAE is trained in an unsupervised way over data, with no knowledge of the signal model.
1190 It is able to perform anomaly detection through an encoder stage which does a lossy compression
1191 on the input to a lower-dimensional latent space, and a decoder stage that samples from that latent
1192 space and generates an output of the original dimensionality. By using the reconstruction error as a
1193 loss, this process enables the VAE to develop a knowledge of the underlying data density, thereby
1194 isolating new out-of-distribution events by their high reconstruction error. We refer to this strategy
1195 as semi-supervised because the tool has some knowledge of correct labels (eg. through the PFN
1196 latent space embedding) but is followed by a data-driven unsupervised stage.

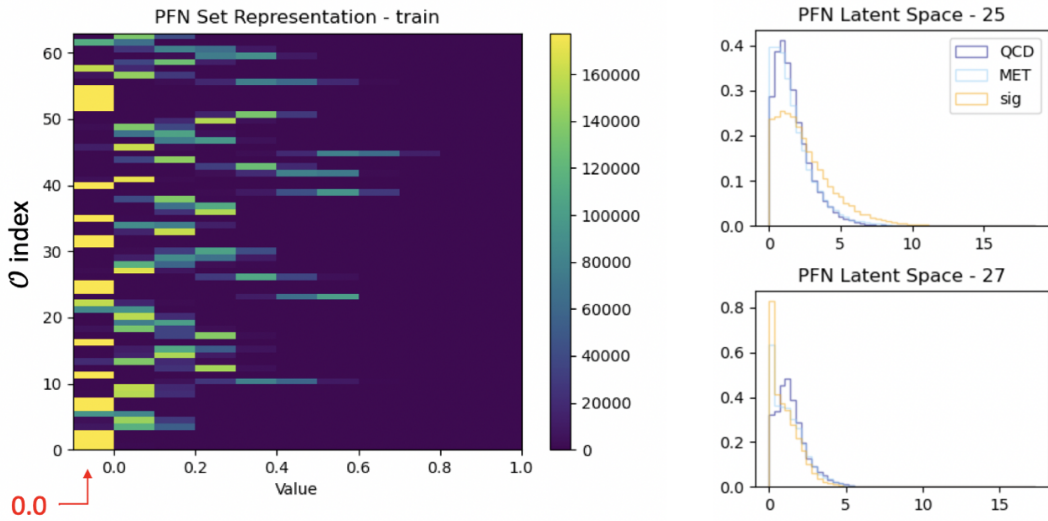


Figure 6.12: A visual representation of the 64 PFN latent space variables which create the input of the VAE component of ANTELOPE. The left shows a 2D histogram of the PFN latent space index (0-63) versus the value assumed by that index. The right shows 1D histograms of two particular PFN latent space variables.

1197 Figure 6.13 provides a diagram of the ANTELOPE architecture.

1198 Training

1199 The VAE stage of the ANTELOPE network is trained directly over a subset of data events at
 1200 preselection (6.7 million available, 200,000 used, with a 80%/20% training/test split). The input
 1201 dimensionality of the VAE has to match the encoded Φ dimension of the PFN, in this case 64.
 1202 The encoder has an encoding layer that brings the dimensionality to 32, and a final layer that
 1203 compresses to the latent space dimension of 12. The network is trained for 50 epochs, with a
 1204 learning rate of 0.00001. The loss \mathcal{L} is the sum of two terms, the mean-squared error (MSE) of
 1205 input-output reconstruction, and the Kullback-Leibler divergence (KLD).

1206 As the PFN inputs are sufficiently normalized to remove any spurious information from train-
 1207 ing, no additional normalization is applied to the PFN encoded inputs. The final ANTELOPE score
 1208 used in the analysis is produced by applying a log + sigmoid transformation function to the total
 1209 evaluated loss \mathcal{L} .

1210 Figure ?? shows the loss during training.

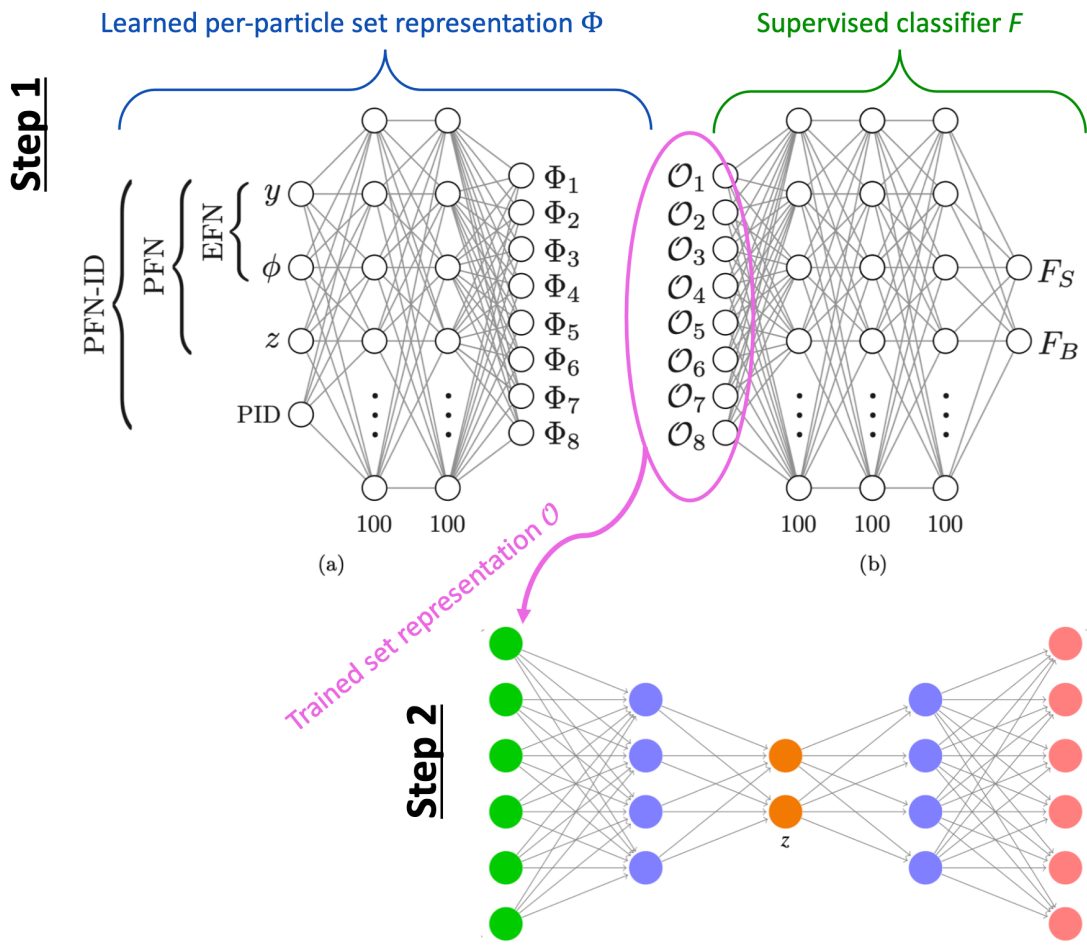


Figure 6.13: An annotated diagram of the ANTELOPE architecture.

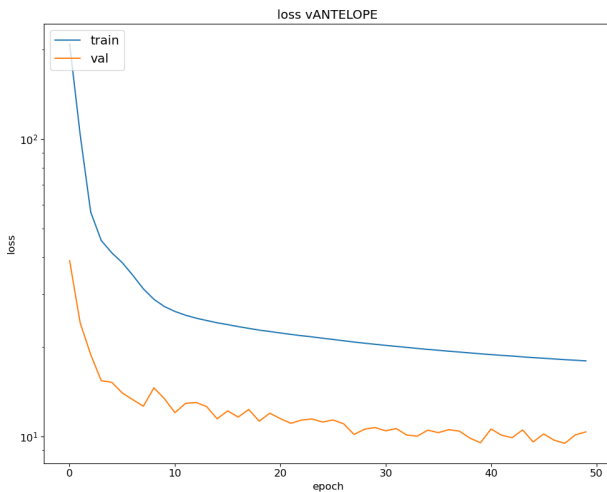


Figure 6.14: ANTELOPE architecture loss during training as a function of epoch.

1211 **Performance**

1212 As with the PFN, the ANTELOPE performance is assessed via the area-under-curve (AUC) of
1213 the receiver operating characteristic (ROC) associated to evaluating the ANTELOPE on the test
1214 set of signal and background events. Figure 6.15 shows the output score distribution in data and
1215 total background MC, showing a very flat ratio and motivating the use of MC for studies of the
1216 ANTELOPE score.

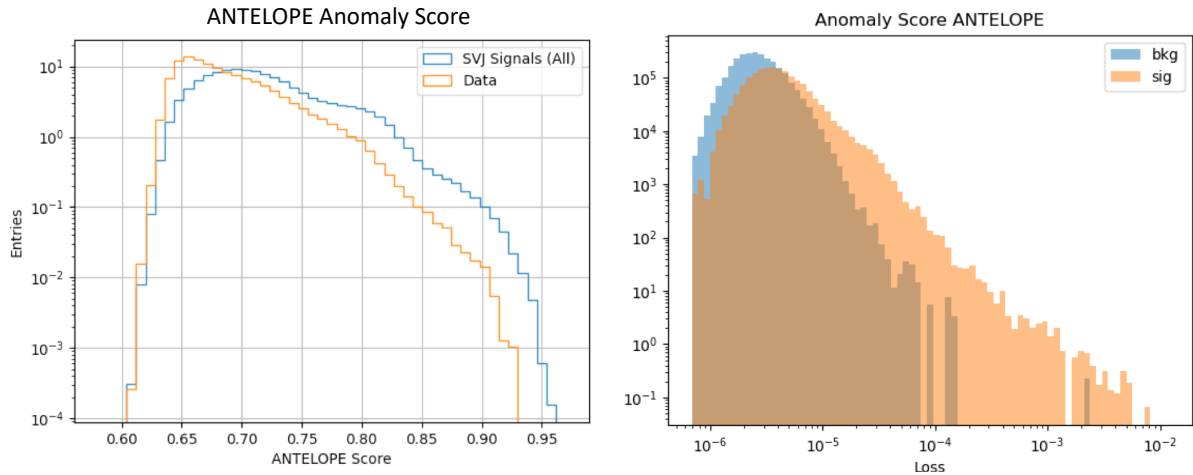


Figure 6.15: ANTELOPE score distribution comparing data and the total background MC (left), with good agreement observed between data and simulated background, and comparing all background MC to signals (right), revealing good discrimination power.

1217 Figure 6.16 shows the AUC of the ANTELOPE across the SVJ signal grid, demonstrating
1218 strong discrimination capability even in the varying corners of phase space. Compared to the
1219 supervised PFN method, the ANTELOPE is not as performant (as expected due to the absence of
1220 signal model in training). However, a selection on events with high ANTELOPE score nonetheless
1221 provides a 10-40% increase in signal significance by removing background and isolating the long
1222 tail of anomalous events.

1223 **Model Independence** The unsupervised component of training the ANTELOPE network is ex-
1224 pected to give it a more generalized sensitivity to new physics with E_T^{miss} and jet activity, beyond
1225 the scope of the SVJ grid. To assess this, alternative signal models are evaluated with the trained

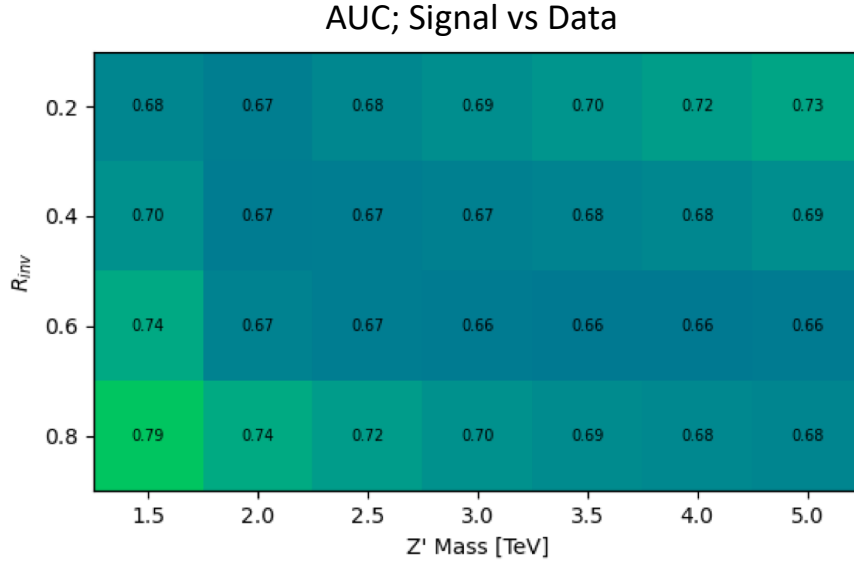


Figure 6.16: AUC from the ANTELOPE score for each signal in the SVJ grid.

1226 ANTELOPE network, as optimized for the SVJ grid, and their sensitivity in the analysis selection
 1227 is evaluated.

1228 The following alternate signal models were considered:

- 1229 • DSID 801661: $Z' \rightarrow t\bar{t}$ (Py8EG_A14NNPDF23LO_Zprime_tt_flatpt)
- 1230 • DSID 801859: $W' \rightarrow WZ$ (Py8EG_A14NNPDF23LO_WprimeWZ_flatpt)
- 1231 • DSIDs 4493???: Gluino pair production \rightarrow R-hadron + LSP (E_T^{miss}) with gluino masses
 1232 2000/3000 GeV, LSP mass 100 GeV, and lifetime 0.03 ns
 1233 (GG_direct_RH_2000_100_0p03ns, GG_direct_RH_3000_100_0p03ns)
- 1234 • DSID 801187: Emerging jets s-channel with mass 1000 GeV and lifetime 1ns
 1235 (EmergingJets_ModelE_1000_1_4jetFilter)

1236 Figure 6.17 shows the distribution of these signals in several key analysis variables, namely
 1237 E_T^{miss} , the PFN score, and the ANTELOPE score. This comparison reveals that ANTELOPE is
 1238 sensitive to E_T^{miss} in the event; it classifies signals with no real E_T^{miss} , like the all-hadronic Z'
 1239 and W' decays (given our imposed lepton veto) as data-like, but the distributions for signals with

1240 E_T^{miss} such as SVJs, R-hadrons, and emerging jets have distributions with higher anomaly score
tails.

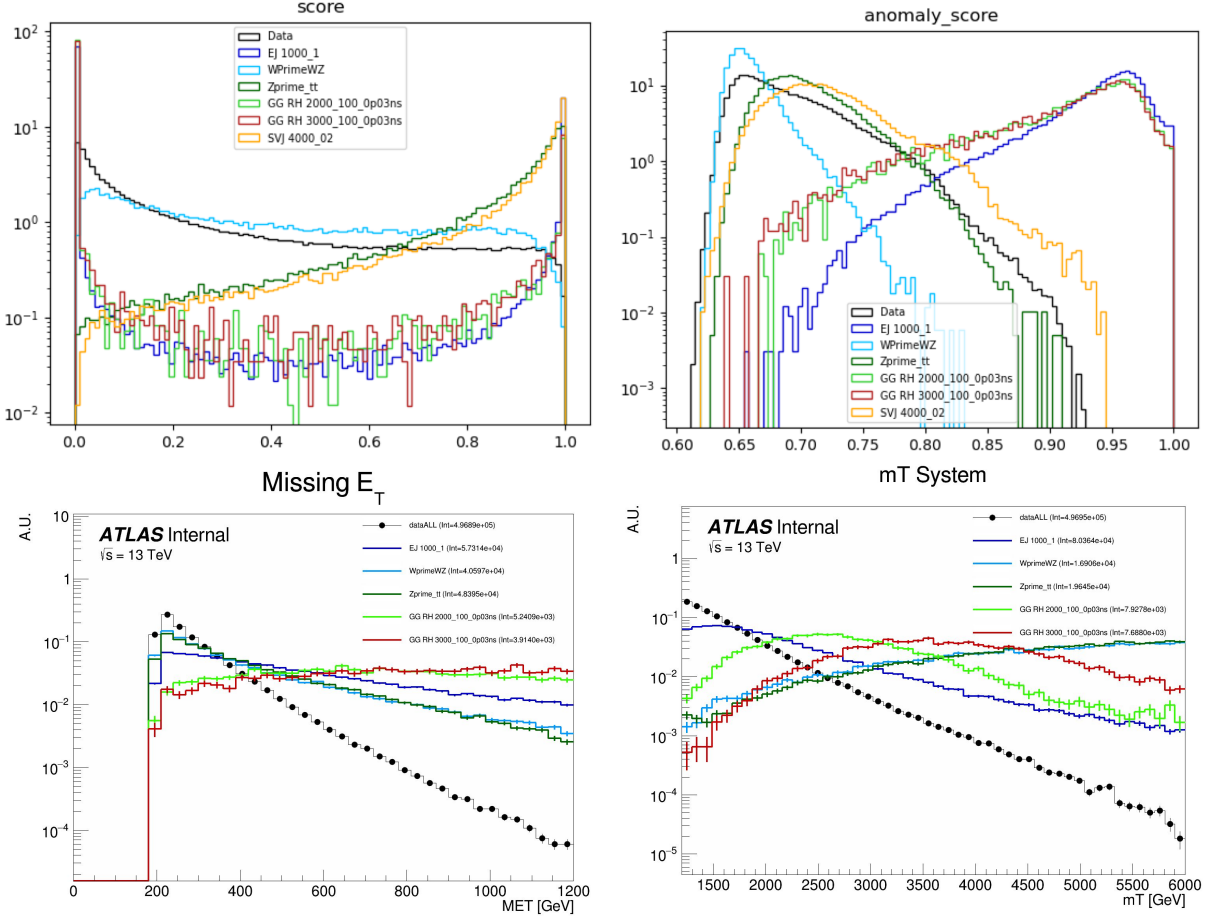


Figure 6.17: Comparing data and the alternate signal models for the PFN score (top left), ANTELOPE score (top right), E_T^{miss} (bottom left), and m_T (bottom right). The emerging jet signal is an example of the gain of the model-independent ANTELOPE approach, where it has a bimodal shape in PFN score but is clearly tagged as anomalous by ANTELOPE.

1241

1242 Figure 6.18 shows a comparison of the sensitivity of the PFN and ANTELOPE regions across
1243 a variety of signals, including the combined SVJ signal used to train the PFN. The benefit of the
1244 unsupervised stage of ANTELOPE in enhancing model independence is clearly seen through the
1245 boost in performance for other signal models, namely the gluino and emerging jet signals, which
1246 have more E_T^{miss} than the W' and Z' signals (all-hadronic) that were also tested. As commented
1247 above, the PFN outperforms ANTELOPE as expected, because it was designed explicitly for the
1248 task of classifying SVJs from background, demonstrating the power of supervised learning for the

1249 model-specific approach.

$\text{sig eff} / \sqrt{\text{bkg eff}}$ for respective score cut (0.6 PFN, 0.7 ANTELOPE)

	EJ 1000	WprimeWZ	Zprime tt	GG RH 2000	GG RH 3000	SVJ
PFN	0.57	0.65	1.92	0.30	0.32	1.97
ANTELOPE	1.73	0.07	0.84	1.72	1.72	1.13

Figure 6.18: Comparing data and the alternate signal models in terms of sensitivity (S/\sqrt{B}) for the PFN and ANTELOPE tools, applying the selection that is used in the analysis. The ANTELOPE network is found to provide significant added sensitivity to alternate signals such as the gluino \rightarrow R-hadron and emerging jets, which have higher E_T^{miss} than the SVJs.

1250 Studies on the ANTELOPE architecture and comparisons to other methods can be found in

1251 Appendix ??.

1252

1253

Chapter 7: Monte Carlo and Data

1254

Conclusion or Epilogue

1255 Use this page for your epilogue or conclusion if applicable; please use only one of the titles
1256 for this page. Otherwise, you may delete it. Use this page for your epilogue or conclusion if
1257 applicable; please use only one of the titles for this page. Otherwise, you may delete it. Use this
1258 page for your epilogue or conclusion if applicable; please use only one of the titles for this page.
1259 Otherwise, you may delete it. Use this page for your epilogue or conclusion if applicable; please
1260 use only one of the titles for this page. Otherwise, you may delete it. Use this page for your
1261 epilogue or conclusion if applicable; please use only one of the titles for this page. Otherwise,
1262 you may delete it. Use this page for your epilogue or conclusion if applicable; please use only one
1263 of the titles for this page. Otherwise, you may delete it. Use this page for your epilogue or
1264 conclusion if applicable; please use only one of the titles for this page. Otherwise, you may delete
1265 it. Use this page for your epilogue or conclusion if applicable; please use only one of the titles for
1266 this page. Otherwise, you may delete it. Use this page for your epilogue or conclusion if
1267 applicable; please use only one of the titles for this page. Otherwise, you may delete it. Use this
1268 page for your epilogue or conclusion if applicable; please use only one of the titles for this page.
1269 Otherwise, you may delete it. Use this page for your epilogue or conclusion if applicable; please
1270 use only one of the titles for this page. Otherwise, you may delete it. Use this page for your
1271 epilogue or conclusion if applicable; please use only one of the titles for this page. Otherwise,
1272 you may delete it. Use this page for your epilogue or conclusion if applicable; please use only one
1273 of the titles for this page. Otherwise, you may delete it. Use this page for your epilogue or
1274 conclusion if applicable; please use only one of the titles for this page. Otherwise, you may delete

1275 it. Use this page for your epilogue or conclusion if applicable; please use only one of the titles for
1276 this page. Otherwise, you may delete it. Use this page for your epilogue or conclusion if
1277 applicable; please use only one of the titles for this page. Otherwise, you may delete it. Use this
1278 page for your epilogue or conclusion if applicable; please use only one of the titles for this page.
1279 Otherwise, you may delete it. Use this page for your epilogue or conclusion if applicable; please
1280 use only one of the titles for this page. Otherwise, you may delete it. Use this page for your
1281 epilogue or conclusion if applicable; please use only one of the titles for this page. Otherwise,
1282 you may delete it. Use this page for your epilogue or conclusion if applicable; please use only one
1283 of the titles for this page. Otherwise, you may delete it. Use this page for your epilogue or
1284 conclusion if applicable; please use only one of the titles for this page. Otherwise, you may delete
1285 it. Use this page for your epilogue or conclusion if applicable; please use only one of the titles for
1286 this page. Otherwise, you may delete it. Use this page for your epilogue or conclusion if
1287 applicable; please use only one of the titles for this page. Otherwise, you may delete it. Use this
1288 page for your epilogue or conclusion if applicable; please use only one of the titles for this page.
1289 Otherwise, you may delete it. Use this page for your epilogue or conclusion if applicable; please
1290 use only one of the titles for this page. Otherwise, you may delete it. Use this page for your
1291 epilogue or conclusion if applicable; please use only one of the titles for this page. Otherwise,
1292 you may delete it. Use this page for your epilogue or conclusion if applicable; please use only one
1293 of the titles for this page. Otherwise, you may delete it. Use this page for your epilogue or
1294 conclusion if applicable; please use only one of the titles for this page. Otherwise, you may delete
1295 it. Use this page for your epilogue or conclusion if applicable; please use only one of the titles for
1296 this page. Otherwise, you may delete it. Use this page for your epilogue or conclusion if
1297 applicable; please use only one of the titles for this page. Otherwise, you may delete it. Use this
1298 page for your epilogue or conclusion if applicable; please use only one of the titles for this page.
1299 Otherwise, you may delete it. Use this page for your epilogue or conclusion if applicable; please
1300 use only one of the titles for this page. Otherwise, you may delete it. Use this page for your
1301 epilogue or conclusion if applicable; please use only one of the titles for this page. Otherwise,

1302 you may delete it. Use this page for your epilogue or conclusion if applicable; please use only one
1303 of the titles for this page. Otherwise, you may delete it. Use this page for your epilogue or
1304 conclusion if applicable; please use only one of the titles for this page. Otherwise, you may delete
1305 it. Use this page for your epilogue or conclusion if applicable; please use only one of the titles for
1306 this page. Otherwise, you may delete it. Use this page for your epilogue or conclusion if
1307 applicable; please use only one of the titles for this page. Otherwise, you may delete it. Use this
1308 page for your epilogue or conclusion if applicable; please use only one of the titles for this page.
1309 Otherwise, you may delete it. Use this page for your epilogue or conclusion if applicable; please
1310 use only one of the titles for this page. Otherwise, you may delete it. Use this page for your
1311 epilogue or conclusion if applicable; please use only one of the titles for this page. Otherwise,
1312 you may delete it. Use this page for your epilogue or conclusion if applicable; please use only one
1313 of the titles for this page. Otherwise, you may delete it. Use this page for your epilogue or
1314 conclusion if applicable; please use only one of the titles for this page. Otherwise, you may delete
1315 it. Use this page for your epilogue or conclusion if applicable; please use only one of the titles for
1316 this page. Otherwise, you may delete it. Use this page for your epilogue or conclusion if
1317 applicable; please use only one of the titles for this page. Otherwise, you may delete it. Use this
1318 page for your epilogue or conclusion if applicable; please use only one of the titles for this page.
1319 Otherwise, you may delete it. Use this page for your epilogue or conclusion if applicable; please
1320 use only one of the titles for this page. Otherwise, you may delete it. Use this page for your
1321 epilogue or conclusion if applicable; please use only one of the titles for this page. Otherwise,
1322 you may delete it. Use this page for your epilogue or conclusion if applicable; please use only one
1323 of the titles for this page. Otherwise, you may delete it. Use this page for your epilogue or
1324 conclusion if applicable; please use only one of the titles for this page. Otherwise, you may delete
1325 it. Use this page for your epilogue or conclusion if applicable; please use only one of the titles for
1326 this page. Otherwise, you may delete it. Use this page for your epilogue or conclusion if
1327 applicable; please use only one of the titles for this page. Otherwise, you may delete it. Use this
1328 page for your epilogue or conclusion if applicable; please use only one of the titles for this page.

1329 Otherwise, you may delete it. Use this page for your epilogue or conclusion if applicable; please
1330 use only one of the titles for this page. Otherwise, you may delete it. Use this page for your
1331 epilogue or conclusion if applicable; please use only one of the titles for this page. Otherwise,
1332 you may delete it. Use this page for your epilogue or conclusion if applicable; please use only one
1333 of the titles for this page. Otherwise, you may delete it. Use this page for your epilogue or
1334 conclusion if applicable; please use only one of the titles for this page. Otherwise, you may delete
1335 it. Use this page for your epilogue or conclusion if applicable; please use only one of the titles for
1336 this page. Otherwise, you may delete it. Use this page for your epilogue or conclusion if
1337 applicable; please use only one of the titles for this page. Otherwise, you may delete it. Use this
1338 page for your epilogue or conclusion if applicable; please use only one of the titles for this page.
1339 Otherwise, you may delete it. Use this page for your epilogue or conclusion if applicable; please
1340 use only one of the titles for this page. Otherwise, you may delete it. Use this page for your
1341 epilogue or conclusion if applicable; please use only one of the titles for this page. Otherwise,
1342 you may delete it. Use this page for your epilogue or conclusion if applicable; please use only one
1343 of the titles for this page. Otherwise, you may delete it. Use this page for your epilogue or
1344 conclusion if applicable; please use only one of the titles for this page. Otherwise, you may delete
1345 it. Use this page for your epilogue or conclusion if applicable; please use only one of the titles for
1346 this page. Otherwise, you may delete it. Use this page for your epilogue or conclusion if
1347 applicable; please use only one of the titles for this page. Otherwise, you may delete it. Use this
1348 page for your epilogue or conclusion if applicable; please use only one of the titles for this page.
1349 Otherwise, you may delete it. Use this page for your epilogue or conclusion if applicable; please
1350 use only one of the titles for this page. Otherwise, you may delete it. Use this page for your
1351 epilogue or conclusion if applicable; please use only one of the titles for this page. Otherwise,
1352 you may delete it. Use this page for your epilogue or conclusion if applicable; please use only one
1353 of the titles for this page. Otherwise, you may delete it. Use this page for your epilogue or
1354 conclusion if applicable; please use only one of the titles for this page. Otherwise, you may delete
1355 it.

References

- [1] Jens Erler and Paul Langacker. “Electroweak model and constraints on new physics”. In: (July 2004). arXiv: hep-ph/0407097.
- [2] David J Griffiths. *Introduction to elementary particles; 2nd rev. version*. Physics textbook. New York, NY: Wiley, 2008.
- [3] M. Tanabashi et al. “Review of Particle Physics”. In: *Phys. Rev. D* 98 (3 2018), pp. 847–851.
- [4] E. Noether. “Invariante Variationsprobleme”. In: *Nachr. d. König. Gesellsch. d. Wiss. zu Göttingen, Math-phys. Klasse*, Seite 235-157 (1918). eprint: www.physics.ucla.edu/\~\cwp/articles/noether.trans/german/emmy235.html.
- [5] J. H. Christenson et al. “Evidence for the 2π Decay of the K_2^0 Meson”. In: *Phys. Rev. Lett.* 13 (1964), pp. 138–140.
- [6] J. E. Augustin et al. “Discovery of a Narrow Resonance in e^+e^- Annihilation”. In: *Phys. Rev. Lett.* 33 (1974), pp. 1406–1408.
- [7] J. J. Aubert et al. “Experimental Observation of a Heavy Particle J ”. In: *Phys. Rev. Lett.* 33 (1974), pp. 1404–1406.
- [8] Martin L. Perl et al. “Evidence for Anomalous Lepton Production in e+ - e- Annihilation”. In: *Phys. Rev. Lett.* 35 (1975), pp. 1489–1492.
- [9] S. W. Herb et al. “Observation of a Dimuon Resonance at 9.5-GeV in 400-GeV Proton-Nucleus Collisions”. In: *Phys. Rev. Lett.* 39 (1977), pp. 252–255.
- [10] F. Abe et al. “Observation of top quark production in $\bar{p}p$ collisions”. In: *Phys. Rev. Lett.* 74 (1995), pp. 2626–2631. arXiv: hep-ex/9503002.
- [11] S. Abachi et al. “Observation of the top quark”. In: *Phys. Rev. Lett.* 74 (1995), pp. 2632–2637. arXiv: hep-ex/9503003.
- [12] K. Kodama et al. “Observation of tau neutrino interactions”. In: *Phys. Lett. B* 504 (2001), pp. 218–224. arXiv: hep-ex/0012035.
- [13] G. Arnison et al. “Experimental Observation of Lepton Pairs of Invariant Mass Around 95-GeV/c**2 at the CERN SPS Collider”. In: *Phys. Lett. B* 126 (1983), pp. 398–410.

- 1383 [14] P. Bagnaia et al. “Evidence for $Z^0 \rightarrow e^+e^-$ at the CERN $\bar{p}p$ Collider”. In: *Phys. Lett. B* 129
 1384 (1983), pp. 130–140.
- 1385 [15] Serguei Chatrchyan et al. “Observation of a New Boson at a Mass of 125 GeV with the
 1386 CMS Experiment at the LHC”. In: *Phys. Lett. B* 716 (2012), pp. 30–61. arXiv: 1207.7235
 1387 [hep-ex].
- 1388 [16] Georges Aad et al. “Observation of a new particle in the search for the Standard Model
 1389 Higgs boson with the ATLAS detector at the LHC”. In: *Phys. Lett. B* 716 (2012), pp. 1–29.
 1390 arXiv: 1207.7214 [hep-ex].
- 1391 [17] K. G. Begeman, A. H. Broeils, and R. H. Sanders. “Extended rotation curves of spiral galaxies:
 1392 Dark haloes and modified dynamics”. In: *Mon. Not. Roy. Astron. Soc.* 249 (1991), p. 523.
- 1393 [18] Y. Ashie et al. “Evidence for an oscillatory signature in atmospheric neutrino oscillation”.
 1394 In: *Phys. Rev. Lett.* 93 (2004), p. 101801. arXiv: hep-ex/0404034.
- 1395 [19] C. Abel et al. “Measurement of the Permanent Electric Dipole Moment of the Neutron”. In:
 1396 *Phys. Rev. Lett.* 124.8 (2020), p. 081803. arXiv: 2001.11966 [hep-ex].
- 1397 [20] Guillaume Albouy et al. “Theory, phenomenology, and experimental avenues for dark showers:
 1398 a Snowmass 2021 report”. In: *The European Physical Journal C* 82.12 (Dec. 2022).
- 1399 [21] Lyndon Evans and Philip Bryant. “LHC Machine”. In: *Journal of Instrumentation* 3.08
 1400 (2008), S08001.
- 1401 [22] “The ATLAS Experiment at the CERN Large Hadron Collider”. In: *JINST* 3 (2008). Also
 1402 published by CERN Geneva in 2010, S08003.
- 1403 [23] “The CMS experiment at the CERN LHC”. In: *Journal of Instrumentation* 3.08 (2008),
 1404 S08004.
- 1405 [24] “The ALICE experiment at the CERN LHC”. In: *Journal of Instrumentation* 3.08 (2008),
 1406 S08002.
- 1407 [25] “The LHCb Detector at the LHC”. In: *Journal of Instrumentation* 3.08 (2008), S08005.
- 1408 [26] Ana Lopes and Melissa Loyse Perrey. *FAQ-LHC The guide*. 2022.
- 1409 [27] Esma Mobs. “The CERN accelerator complex in 2019. Complexe des accélérateurs du
 1410 CERN en 2019”. In: (2019). General Photo.
- 1411 [28] *Pulling together: Super Conducting electromagnets*. <https://home.cern/science/engineering/pulling-together-superconducting-electromagnets>.
 1412 Accessed: 2024-01-05.

- 1414 [29] *The High-Luminosity LHC*. <https://voisins.web.cern.ch/en/high-luminosity-lhc-hl-lhc>. Accessed: 2024-01-05.
- 1415
- 1416 [30] Aad G., et al. (ATLAS Collaboration and CMS Collaboration). “Combined Measurement of
1417 the Higgs Boson Mass in pp Collisions at $\sqrt{s} = 7$ and 8 TeV with the ATLAS and CMS
1418 Experiments”. In: *Phys. Rev. Lett.* 114 (19 2015), p. 191803.
- 1419 [31] O. Aberle et al. *High-Luminosity Large Hadron Collider (HL-LHC): Technical design re-*
1420 *port*. CERN Yellow Reports: Monographs. Geneva: CERN, 2020.
- 1421 [32] The ATLAS Collaboration. “The ATLAS Experiment at the CERN Large Hadron Collider”.
1422 In: *Journal of Instrumentation* 3.08 (2008), S08003.
- 1423 [33] G Aad, B Abbott, and ATLAS Collaboration. “Performance of the reconstruction of large
1424 impact parameter tracks in the inner detector of ATLAS”. In: *Eur. Phys. J. C Part. Fields*
1425 83.11 (Nov. 2023).
- 1426 [34] Joao Pequenao. *Computer Generated image of the ATLAS calorimeter*. 2008.
- 1427 [35] *ATLAS liquid-argon calorimeter: Technical Design Report*. Technical design report. AT-
1428 LAS. Geneva: CERN, 1996.
- 1429 [36] H A Gordon. “Liquid argon calorimetry for the SSC”. In: () .
- 1430 [37] Henric Wilkens and (on behalf of the ATLAS LArg Collaboration). “The ATLAS Liquid
1431 Argon calorimeter: An overview”. In: *Journal of Physics: Conference Series* 160.1 (2009),
1432 p. 012043.
- 1433 [38] *Technical Design Report for the Phase-II Upgrade of the ATLAS Tile Calorimeter*. Tech.
1434 rep. Geneva: CERN, 2017.
- 1435 [39] “Technical Design Report for the Phase-II Upgrade of the ATLAS Muon Spectrometer”. In:
1436 () .
- 1437 [40] L Pontecorvo. “The ATLAS Muon Spectrometer”. In: (2004). revised version number 1
1438 submitted on 2003-07-27 16:31:16.
- 1439 [41] *ATLAS magnet system: Technical Design Report, 1*. Technical design report. ATLAS. Geneva:
1440 CERN, 1997.
- 1441 [42] Joao Pequenao. “Event Cross Section in a computer generated image of the ATLAS detec-
1442 tor.” 2008.
- 1443 [43] ATLAS Collaboration. “ATLAS Experiment Implements Heterogeneous Particle Recon-
1444 struction with Intel oneAPI Tools”. General Photo. 2023.

- 1445 [44] ATLAS Collaboration. “Electron and photon performance measurements with the ATLAS
 1446 detector using the 2015–2017 LHC proton-proton collision data”. In: *Journal of Instrumentation*
 1447 14.12 (2019), P12006.
- 1448 [45] Chiara Deponte. “Studies on the properties of non-prompt photons at the ATLAS experi-
 1449 ment”. Presented 16 Aug 2022. Technische Universitaet Dortmund (DE), 2022.
- [46] ATLAS Collaboration. “Muon reconstruction performance of the ATLAS detector in pro-
 ton–proton collision data at
 \sqrt{s}
 1450 $s = 13 \text{ TeV}$ ”. In: *The European Physical Journal C* 76.5 (2016).
- 1451 [47] Sebastien Rettie. *Muon identification and performance in the ATLAS experiment*. Tech. rep.
 1452 Geneva: CERN, 2018.
- 1453 [48] B. R. Webber. *Fragmentation and Hadronization*. 1999. arXiv: hep-ph/9912292 [hep-ph].
- 1454 [49] Eric M. Metodiev. *The Fractal Lives of Jets | Eric M. Metodiev — ericmetodiev.com*. <https://www.ericmetodiev.com/post/jetformation/>. 2019, note = [Accessed 18-
 1455 05-2024],
- 1456 [50] Matteo Cacciari, Gavin P Salam, and Gregory Soyez. “The anti-ktjet clustering algorithm”.
 1457 In: *Journal of High Energy Physics* 2008.04 (Apr. 2008), 063–063.
- 1459 [51] Matteo Cacciari, Gavin P. Salam, and Gregory Soyez. “FastJet user manual: (for version
 1460 3.0.2)”. In: *The European Physical Journal C* 72.3 (Mar. 2012).
- 1461 [52] Steven Schramm. *ATLAS Jet Reconstruction, Calibration, and Tagging of Lorentz-boosted
 1462 Objects*. Tech. rep. Geneva: CERN, 2017.
- 1463 [53] ATLAS Collaboration. “Topological cell clustering in the ATLAS calorimeters and its per-
 1464 formance in LHC Run 1”. In: *The European Physical Journal C* 77.7 (July 2017).
- 1465 [54] ATLAS Collaboration. “Jet reconstruction and performance using particle flow with the
 1466 ATLAS Detector”. In: *The European Physical Journal C* 77.7 (July 2017).
- 1467 [55] Stephen D. Ellis and Davison E. Soper. “Successive combination jet algorithm for hadron
 1468 collisions”. In: *Physical Review D* 48.7 (Oct. 1993), 3160–3166.
- 1469 [56] M. Wobisch and T. Wengler. *Hadronization Corrections to Jet Cross Sections in Deep-
 1470 Inelastic Scattering*. 1999. arXiv: hep-ph/9907280 [hep-ph].
- 1471 [57] Gavin P Salam and Gr  gory Soyez. “A practical seedless infrared-safe cone jet algorithm”.
 1472 In: *Journal of High Energy Physics* 2007.05 (May 2007), 086–086.

- 1473 [58] Gavin P. Salam. “Towards jetography”. In: *The European Physical Journal C* 67.3–4 (May
1474 2010), 637–686.
- 1475 [59] *A Monte Carlo study of track association to jets for b-tagging*. Tech. rep. Geneva: CERN,
1476 2021.
- 1477 [60] *Flavor Tagging with Track Jets in Boosted Topologies with the ATLAS Detector*. Tech. rep.
1478 All figures including auxiliary figures are available at <https://atlas.web.cern.ch/Atlas/GROUPS/PHYSICS/P>
1479 PHYS-PUB-2014-013. Geneva: CERN, 2014.
- 1480 [61] ATLAS Collaboration. “Performance of missing transverse momentum reconstruction with
1481 the ATLAS detector using proton-proton collisions at $\sqrt{s} = 13$ TeV”. In: *Eur. Phys. J. C*
1482 78.11 (2018), p. 903. arXiv: 1802 . 08168.

1483

1484

Appendix A: Experimental Equipment

1485 Lorem ipsum dolor sit amet, consectetur adipiscing elit, sed do eiusmod tempor incididunt ut
1486 labore et dolore magna aliqua. Ut enim ad minim veniam, quis nostrud exercitation ullamco laboris
1487 nisi ut aliquip ex ea commodo consequat. Duis aute irure dolor in reprehenderit in voluptate velit
1488 esse cillum dolore eu fugiat nulla pariatur. Excepteur sint occaecat cupidatat non proident, sunt in
1489 culpa qui officia deserunt mollit anim id est laborum.

1490

1491

Appendix B: Data Processing

1492 Lorem ipsum dolor sit amet, consectetur adipiscing elit, sed do eiusmod tempor incididunt ut
1493 labore et dolore magna aliqua. Ut enim ad minim veniam, quis nostrud exercitation ullamco laboris
1494 nisi ut aliquip ex ea commodo consequat. Duis aute irure dolor in reprehenderit in voluptate velit
1495 esse cillum dolore eu fugiat nulla pariatur. Excepteur sint occaecat cupidatat non proident, sunt in
1496 culpa qui officia deserunt mollit anim id est laborum.